A Dissertation for the Degree of Doctor of Philosophy

Biophysical Characterization of Interaction Between Domain A and B of the Mannitol Transporter Enzyme II by NMR Spectroscopy

핵자기 공명 분광학을 이용한 마니톨 운반 효소 II의 도메인 A와 B의 상호작용에 관한 생물리학적 특성 연구

February, 2017

Biomodulation Major

Department of Agricultural Biotechnology

Seoul National University

Ko On Lee

Biophysical Characterization of Interaction Between Domain A and B of the Mannitol Transporter Enzyme II by NMR Spectroscopy

핵자기 공명 분광학을 이용한 마니톨 운반 효소 II의 도메인 A와 B의 상호작용에 관한 생물리학적 특성 연구

지도교수 서 정 용

이 논문을 이학박사학위논문으로 제출함
2016년 12월

서울대학교 대학원
농생명공학부 바이오모듈레이션 전공

이 고 은

이고은의 박사학위논문을 인준함
2016년 12월

위 원 장 _____ 석차옥 (인)

부 위 원 장 _____ 서정용 (인)

위 원 _____ 이상기 (인)

위 원 _____ 최희정 (인)

위 원 _____ 김낙균 (인)

ABSTRACT

Biophysical characterization of the interaction between domains A and B of the mannitol transporter enzyme II by NMR spectroscopy

Ko On Lee

Biomodulation Major

Department of Agricultural Biotechnology

Seoul National University

In multi-domain proteins, protein linkers serve to maintain separate domains within a certain distance, and also affect the domain-domain motion. The cytoplasmic A and B domains of mannitol transporter enzymes are well-conserved across bacterial strains. Domain A and B are covalently connected by a flexible linker in *Escherichia coli*, whereas they are separated in the thermophilic bacterium *Thermoanaerobacter Tengcongensis* (*Tt*). In this study, I investigated changes in domain association changes when the domains have evolved with or without their connecting linkers by characterizing the structure and interaction of the *Tt* mannitol transporter A (TtIIA^{mtl}) and phosphorylated B (phospho-TtIIB^{mtl}) domains. The backbone folds and interface of individual domains were well conserved between the two bacterial strains. However, separated domains showed 28 times higher affinity than the linked ones. The increase in binding affinity mainly resulted from

different compositions of interfacial residues, with the general backbone fold of the complex remaining unperturbed. Phosphorylation of the active site loop significantly contributed to the binding affinity by reducing conformational dynamics at the binding interface, and a few key mutations at the interface were sufficient to account for the enhanced binding affinity. Specifically, the complex was stabilized by extended hydrophobic interactions through T542I and P543T and from hydrogen bonds between the hydroxyl group of V557S and the carboxyl backbone group of A386, which enhances the affinity thereby enabling a proper domain association regardless of the presence of the linker. Interestingly, the population of the association state *in vivo* was estimated to be nearly identical between the non-linked and linked domains. These results suggest that the binding affinity between domains is, modulated in response to changes in the connecting linkers, which would help to maintain the domain association at a functional level regardless of the presence of the linker.

Key words : domain association, domain interface, Mannitol transporter enzyme II, linker, multi-domain protein, nuclear magnetic resonance spectroscopy

Student Number: 2010-30826

CONTENTS

LIST OF FIGURES

LIST OF TABLES

ABBREVIATION

βME	beta‑Mercaptoethanol
CBCACONH	Correlation spectroscopy for H^N-N^H-$C\alpha^i$-$C\beta^i$
CSP	Chemical shift perturbation
DEAE	Diethlamnioethyl
Ec	*Escherichia coli*
HNCACB	Correlation spectroscopy for $C\alpha^{i-1}$-$C\beta^{i-1}$ -H^N-N^H-$C\alpha^i$-$C\beta^i$
HSQC	Heteronuclear single quantum coherence spectroscopy
IIA^{Mtl}	Domain A of Enzyme II mannitol transporter
IIB^{Mtl}	Domain B of Enzyme II mannitol transporter
ITC	Isothermal titration calorimetry
K_D	Equilibrium dissociation constant
NMR	Nuclear magnetic resonance
OD	Optical density
PCR	Polymerase Chain Reaction
PEP	Phosphoenolpyruvate
PTS	Phosphotransferase system
SDS-PAGE	Sodium dodecyl sulfate-polyacrylamide gel electrophoresis
TEV	Tobacco Etch Virus
Tt	*Thermoanaerobacter tengcongensis*
RDC	Residual dipolar coupling

1. Introduction

1.1 Role of the linker in protein-protein interactions

Fundamental biological processes such as enzyme catalysis, metabolism, signal transduction, and gene regulations are mediated by molecular recognition. Molecular recognition is highly specified for a given binding partner or for binding to many non-obligatory partners whose function will be disturbed. Protein-protein interactions between the proteins are mainly achieved by the structural complementation of their interacting surfaces including appropriate shape, volume of the molecules and non-covalent interactions (i.e., hydrogen-bonding, salt bridges, and van der Waals, hydrophobic, and π-interactions). In addition, the dynamic behaviors[1, 2] interplay with protein interactions to achieve proper function.

The central unit of the protein interactions is a domain that also serves as the functional and structural unit of a protein. In addition, the domain is the central unit in the evolution of diverse proteins and requires all composition partner domains to carry out the activity[3]. Protein linkers connect a multi-domain protein to maintain separate domains together and to also restrict domain motions in a certain geometrical manner for prohibiting unwanted interactions[4, 5]. Domain linkers have been hypothesized to provide a flexible region to the protein which results in increasing in the distance between active domains[6–9,] presumably to optimize the interaction with substrates. A flexible linker that does not interrupt the interaction between the domains effectively increases the local concentration of individual domains, enabling a significant stable complex formation with millimolar range or stronger dissociating domains[4].

1.2 Post-translational modification (PTM)

After a polypeptide has been synthesized from the ribosome, some of the amino acid side chains may be modified and act as important components in biological processes. PTMs can occur on the sidechain of many amino acids with diverse chemical groups such as methylation, acetylation, glycosylation, carboxylation, oxidation, lipidation, hydroxylation and phosphorylation. In some cases, a specific modification of amino acids in a protein enables proper enzymatic activity, alters the activity level, changes the conformation and surface charge of a protein, and can ultimately alter the activity.

Among the PTMs, phosphorylation is a very common mechanism for regulating protein the activity[11] in both prokaryotic and eukaryotic organisms. It is estimated that up to 30% of proteins in a mammalian cell are phosphorylated.[12] During phosphorylation, a phosphate group is attached to the several nucleophilic sidechains in a reversible manner, enabling switching the protein functions. Serine, threonine, and tyrosine form a phosphomonoester bonds, whereas histidine, arginine, or lysine forms a phosphoramidate P–N bond. Furthermore, aspartate and glutamate forms acyl phosphate, while phosphorylated cysteine forms a phosphorothiolate P–S bond.[13] The different thermodynamic and kinetic properties of the chemical bonds between the phosphoryl group and the respective amino acid can result in altered kinetic stability and transfer potential of these phosphate groups. Reversible protein phosphorylation plays regulatory roles in almost every basic cellular process, including metabolism, enzyme inhibition[14], protein recognition[15], signaling networks[16], stress response[17], transcription[18], differentiation[19], organelle trafficking[20], membrane transport[21], muscle contraction[22], and protein degradation.[23] Reversible phosphorylation also results in a conformational change[24] in the structure of many enzymes and receptors, causing them to become activated or deactivated.

1.3 Mannitol transporter enzyme II^{Mtl}

The phosphotransferase system (PTS)[25-27] constitutes a central signaling network for sugar uptake and phosphorylation in bacteria. The PTS is composed of two universal phosphotransferases, enzyme I and HPr, and sugar-specific transporters, enzymes II. Enzyme I transfers a phosphoryl group from phosphoenolpyruvate to the phosphocarrier protein HPr, and HPr delivers the phosphoryl group to enzymes II. Enzymes II are sugar-specific transmembrane permeases[28, 29] comprising three or four domains that are linked or separated depending on the bacterial strain and sugar specificity. Enzymes II are comprised of cytoplasmic IIA and IIB domains as well as a transmembrane IIC or IIDC domain. Mannitol transporter enzyme II^{Mtl} belongs to the bacterial phosphotransferase system for sugar uptake and metabolism, which is conserved across bacterial strains. In the mannitol transporter system, the phosphoryl group is sequentially transferred from HPr to IIA^{Mtl}, then to IIB^{Mtl}, and finally to an incoming sugar molecule bound on IIC^{Mtl}.[30] The three domains of enzyme II^{Mtl} are expressed as a single polypeptide[31] ($IICBA^{Mtl}$) in *Escherichia. coli.*

The structures of the individual IIA^{Mtl} (PDB entry 1A3A)[31] and IIB^{Mtl} domains (PDB entry 1VRV, 1VKR)[32, 33] of *E. coli* and their complex[34] (PDB entry 2FEW, Fig.1) have been previously determined by X-ray crystallography and nuclear magnetic resonance (NMR) spectroscopy. *Ec*IIA^{Mtl} is composed of a central five-stranded beta-sheet flanked by five alpha-helices[31, 34], and *Ec*IIB^{Mtl} is composed of a central four-stranded beta-sheet, flanked by three alpha-helices. Comparison of isolated unphsopho–IIB^{Mtl} and phospho–IIB^{Mtl} structures showed that phosphorylation does not perturbed the global structure at all[34] (Fig. 2). However, a minute difference occurred by additional hydrogen bonding between the active site loop and phosphoryl group to stabilizes the phosphorylated IIB^{Mtl}.

It has been reported that *Ec*IIA^{Mtl} and *Ec*IIB^{Mtl} form a very weak complex with an equilibrium dissociation constant (K_D) of 3.7 mM. The intrinsically low affinity is compensated by a native connecting linker.[34] At first glance, the intrinsic affinity may seem to be prohibitively weak to elicit a meaningful biological response, however, the domains are naturally connected by a flexible linker that substantially increases the effective local concentration. Specifically, the presence of an unstructured 21-residue linker between IIA^{Mtl} and IIB^{Mtl} of *E. coli* raises the effective concentration up to 4 mM[34], so that the fraction of the associated state can be maintained at ~40% in the single-chain IIBA^{Mtl}.[36]

The mannitol transporter enzymes of the mesophilic gram-negative bacteria are expressed in a single peptide. In a similar vein, *E. coli* mannitol transporter enzyme has a single poly peptide (*Ec*IICBA^{Mtl}), The linkers between IICB^{Mtl} and IIA^{Mtl} are made up by nearly 23 residues for linker that has a similar distance restraint. Whereas thermophilic bacteria, *Bacillus subtilis* and *Thermoanaerobacter tengcongensis* (*T. t*) have two separate polypeptides (IICB^{Mtl} and IIA^{Mtl})[37] (Figs. 3 and 4). IICB^{Mtl} is highly conserved between *E. coli* and *T. t* with a 49% identity, whereas the sequence of IIA^{Mtl} shows more substantial alternation, with only 38% sequence identity[38]. Considering that PTS proteins in the cell exist in a low micromolar range[39], the fractional population of the association state between separated IIA^{Mtl} and IIB^{Mtl} becomes negligible when the K_D value lies in a millimolar range similar to that of the linked domains.

In this study, the backbone folds of *Tt*IIA^{Mtl} and *Tt*IIB^{Mtl} were elucidated by backbone assignment residual dipolar coupling (RDC) and the interaction between the domains was examined using NMR titration and Isothermal titration calorimetry (ITC). The results showed that the backbone folds and interface of individual domains were well conserved between the two bacterial strains. However, the

*Tt*IIA^{Mtl}–phospho-*Tt*IIB^{Mtl} complex showed 28 times higher affinity than the linked domains. Further mutational analysis demonstrated that the complex was stabilized by local chemistry alternation through expanded hydrophobic interactions and hydrogen bonds between tdomains. The enhanced affinity enables maintenance of a proper domain association level regardless of the presence of the linker.

Figure 1. Complex structure of the enzyme IIA^{Mtl} and phosphorylated IIB^{Mtl}.

Complex structure of the enzyme IIA^{Mtl} (cyan) and phosphorylated IIB^{Mtl} (green) complex from *Escherichia coli* (PDB entry 2FEW)[34] has shown in ribbon diagram. Active site residues phospho-IIB^{Mtl} (C384S) and IIA^{Mtl} (His554) are shown in stick. Labeling of secondary structure is indicated.

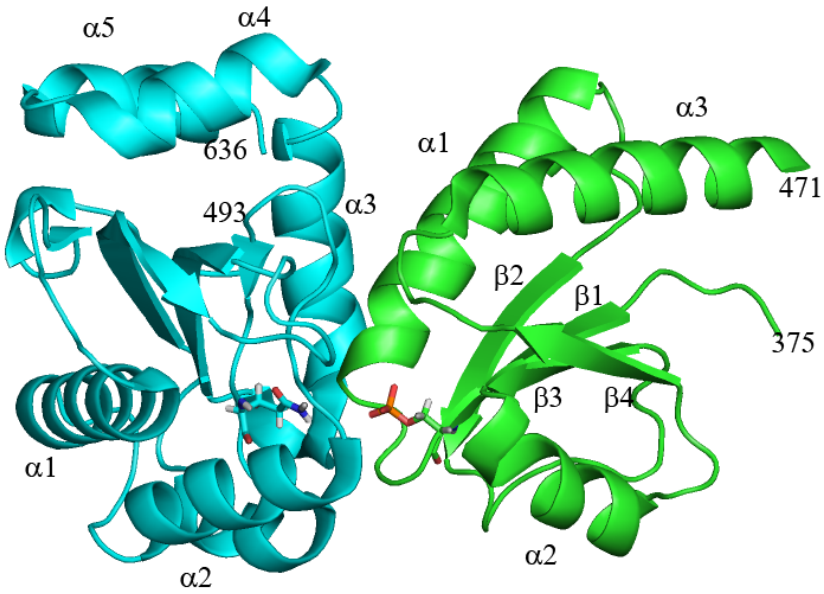
α5
α4
636
493
α3
α1
α2
α1
α3
471
β2
β1
375
β3
β4
α2

Figure 2. The structure of unphosphorylated IIB^{Mtl} and phospho-IIB^{Mtl}

(A) Structure of the unphosphorylated IIB^{Mtl} (cyan) (PDB entry 1VKR)[32] and phospho-IIB^{Mtl} (orange) (PDB entry 1VRV)[33] are superimposed and shown in ribbon diagram. Active site residue of phospho-IIB^{Mtl} (C384S) is shown in stick and active site loop residues are shown in line. (B) Active site of unphosphorylated IIB^{Mtl} (PDB entry 1VKR)[32] and (C) phospho-IIB^{Mtl} (PDB entry 1VRV)[33]. Unphosphorylated IIB^{Mtl} and phospho-IIB^{Mtl} are shown in close view. Active site loop residues are shown in line and the hydrogen bond that is responsible for the phosphorylation state are shown in stick.

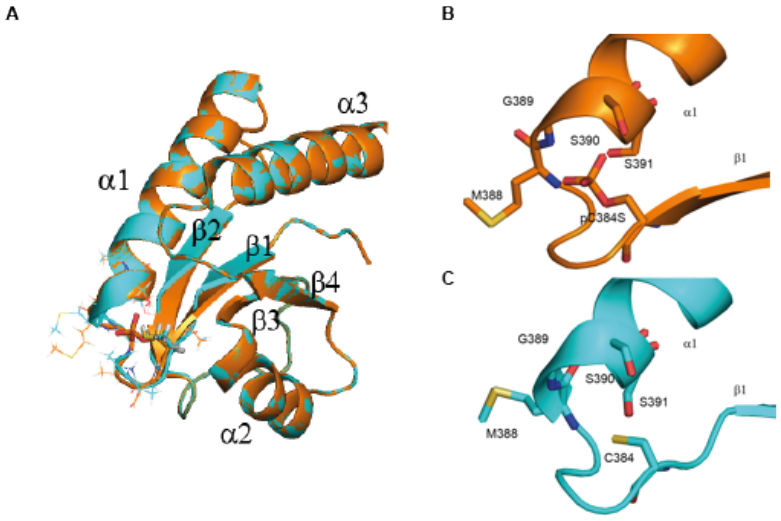
A
α3
α1
β2
β1
β4
β3
α2
B
G389
α1
S390
S391
β1
M388
C384S
C
G389
α1
S390
S391
β1
M388
C384

Figure 3. Transportation of mannitol by the PEP-dependent phosphotransferase system (PTS) in *E.coli* (upper panel) and in *T.tengcongensis* (lower panel)

HPr and EI are cytoplasmic proteins common to all sugars transported. IIA and IIB are enzyme transporter specific for mannitol. *Ec*II^{Mtl} is consisted of transmembrane domain C, domain B and domain A connected by linkers as a single protein. *Tt*II^{Mtl} is consisted of transmembrane domain C connected with domain B by a linker, and domain A has separately expressed in a single protein

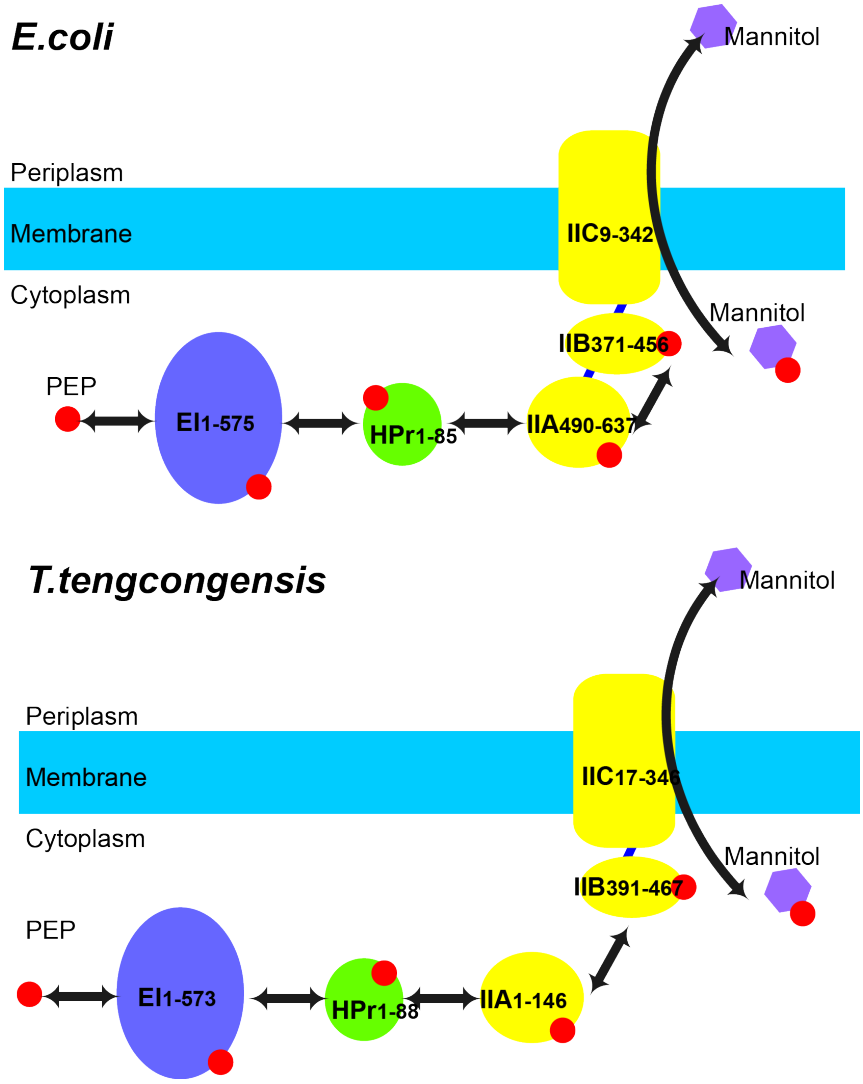
E.coli
Mannitol
Periplasm
Membrane
IIC9-342
Cytoplasm
Mannitol
IIB371-456
PEP
EI1-575
HPr1-85
IIA490-637
T.tengcongensis
Mannitol
Periplasm
Membrane
IIC17-34
Cytoplasm
Mannitol
IIB391-467
PEP
EI1-573
HPr1-88
IIA1-146

Figure 4. Multiple sequence alignment of naturally expressed domain IIBA^{Mtl} and IIB^{Mtl} between *Thermoanaerobacter tengcongensis*, *Escherichia coli*, *Yersinia pestis*, *Vibrio natriegens*, and *Bacillus. subtilis*.

The residue number of separately expressed strains, *Thermoanaerobacter tengcongensis* and *B. subtilis*, are shown in the alignment. Secondary structural elements are displayed above the sequence and 21 residues (*E.coli)*, 26 residues (*Y.pestis*) and 23 residues (*V.natriegens*) of domain connecting linkers are colored with green box.

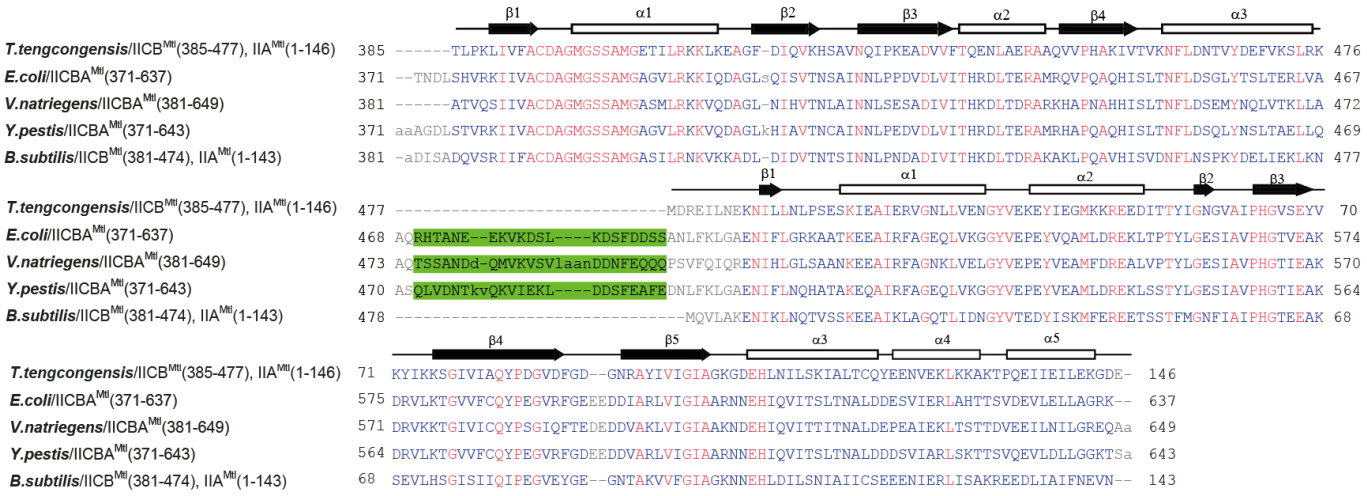
β1 α1 β2 β3 α2 β4 α3
T.tengcongensis/IICBMtl(385-477), IIAMtl(1-146) 385 ------TLPKLIVFACDAGMGSSAMGETILRKKLKEAGF-DIQVKHSAVNQIPKEADVVFTQENLAERAAQVVPHAKIVTVKNFLDNTVYDEFVKSLRK 476
E.coli/IICBAMtl(371-637) 371 --TNDLSHVRKIIVACDAGMGSSAMGAGVLRKKIQDAGLsQISVTNSAINNLPPDVDLVITHRDLTERAMRQVPQAQHISLTNFLDSGLYTSLTERLVA 467
V.natriegens/IICBAMtl(381-649) 381 ------ATVQSIIVACDAGMGSSAMGASMLRKKVQDAGL-NIHVTNLAINNLSESADIVITHKDLTDRAKHAPNAHHISLTNFLDSEMYNQLVTKLLA 472
Y.pestis/IICBAMtl(371-643) 371 aaAGDLSTVRKIIVACDAGMGSSAMGAGVLRKKVQDAGLkHIAVTNCAINNLPEDVDLVITHRDLTERAMRHAPQAQHISLTNFLDSQLYNSLTAELLQ 469
B.subtilis/IICBMtl(381-474), IIAMtl(1-143) 381 -aDISADQVSRIIFACDAGMGSSAMGASILRNKVKKADL-DIDVTNTSINNLPNDADIVITHKDLTDRAKAKLPQAVHISVDNFLNSPKYDELIEKLKN 477
β1 α1 α2 β2 β3
T.tengcongensis/IICBMtl(385-477), IIAMtl(1-146) 477 ----------MDREILNEKNILLNLPSESKIEAIERVGNLLVENGYVEKEYIEGMKKREEDITTYIGNGVAIPHGVSEYV 70
E.coli/IICBAMtl(371-637) 468 AQRHTANE--EKVKDSL----KDSFDDSSANLFKLGAENIFLGRKAATKEEAIRFAGEQLVKGGYVEPEYVQAMLDREKLTPTYLGESIAVPHGTVEAK 574
V.natriegens/IICBAMtl(381-649) 473 AQTSSANDd-QMVKVSVlaanDDNFEQQQPSVFQIQRENIHLGLSAANKEEAIRFAGNKLVELGYVEPEYVEAMFDREALVPTYLGESIAVPHGTIEAK 570
Y.pestis/IICBAMtl(371-643) 470 ASQLVDNTkvQKVIEKL----DDSFEAFEDNLFKLGAENIFLNQHATAKEQAIRFAGEQLVKGGYVEPEYVEAMLDREKLSSTYLGESIAVPHGTIEAK 564
B.subtilis/IICBMtl(381-474), IIAMtl(1-143) 478 ----------MQVLAKENIKLNQTVSSKEEAIKLAGQTLIDNGYVTEDYISKMFEREETSSTFMGNFIAIPHGTEEAK 68
β4 β5 α3 α4 α5
T.tengcongensis/IICBMtl(385-477), IIAMtl(1-146) 71 KYIKKSGIVIAQYPDGVDFGD--GNRAYIVIGIAGKGDEHLNILSKIALTCQYEENVEKLKKAKTPQEIIEILEKGDE- 146
E.coli/IICBAMtl(371-637) 575 DRVLKTGVVFCQYPEGVRFGEEEDDIARLVIGIAARNNEHIQVITSLTNALDDESVIERLAHTTSVDEVLELLAGRK-- 637
V.natriegens/IICBAMtl(381-649) 571 DRVKKTGIVICQYPSGIQFTEDEDDVAKLVIGIAAKNDEHIQVITTITNALDEPEAIEKLTSTTDVEEILNILGREQAa 649
Y.pestis/IICBAMtl(371-643) 564 DRVLKTGVVFCQYPEGVRFGDEEDDVARLVIGIAARNNEHIQVITSLTNALDDDSVIARLSKTTSVQEVLDLLGGKTSa 643
B.subtilis/IICBMtl(381-474), IIAMtl(1-143) 68 SEVLHSGISIIQIPEGVEYGE--GNTAKVVFGIAGKNNEHLDILSNIAIICSEEENIERLISAKREEDLIAIFNEVN-- 143

2 Materials and Methods

2. 1. Cloning

2.1.1 Bacterial strains and plasmids

Each gene of *Tt*HPr (residues 1–88), *Tt*IIA^{Mtl} (1-146) and *Tt*IIB^{Mtl} (385-146) was PCR-amplified from *Thermoanaerobacter Tengcongensis* genomic with the primers (Table 1). *Escherichia coli* DH5α strain was used for DNA manipulation. *Tt*HPr protein coding sequences was PCR amplified using DNA *pfu*Tag polymerase (Stratagene). The PCR products were digested by *NdeI* (Thermo Fisher Scientific) and *XhoI* (Thermo Fisher Scientific) restriction enzyme and sub-cloned into the modified pET-11a with N-terminal His_6 tag. *Tt*IIA^{Mtl} and *Tt*IIB^{Mtl} protein coding sequences were PCR amplified using DNA *pfu*Tag polymerase (Stratagene). The PCR products were digested by *NcoI* (Thermo Fisher Scientific) and *XhoI* (Thermo Fisher Scientific) restriction enzyme and sub-cloned into the modified pET-32a vector with N-terminal His_6 -Trx tag separated by a Tobacco Etch Virus (TEV) cleavage site. The disulfide bonding residue, *Tt*IIA^{Mtl} Cys-119, was mutated to Ala and the active site residue, *Tt*IIB^{Mtl} Cys-384, was mutated to Ser for stabilizing the phosphoryl-group by using the QuikChange kit (Agilent Technologies). For further mutational study, selected interfacial residues were introduced by QuikChange (Agilent Technologies, Inc.) with the PCR primer introduced (Table 2). The new constructs were verified by DNA sequencing.

Table 1. PCR Primers used for template gene insertion to the expression vector.

Construct	Primers	
H_6-*Tt*HPr[a]	forward 5'	CACCATGCATCACCATCACCATCACGGTTCTATGAAAGAAGTTACT
	reverse 3'	GGCTCGAGTTATTACTCTTCACCGAACTTTGA
*Tt*IIA^{Mtl} [b]	forward 5'	CACCATGGCCGAAAACCTGTATTTTCAGGGAATGGACAGAGAAATT
	reverse 3'	GCGGGCTCGAGTTATTACTCATCACCTTTCTCCAG
*Tt*IIB^{Mtl} [b]	forward 5'	GTGCCACGCGGTTCTAAAATGGATACCCTGCCGAAACTC
	reverse 3'	GAGTTTCGGCAGGGTATCCATTTTAGAACCGCGTGGCAC

[a]This primer is designed for the insertion of HPr gene from the target genome *Tt* to modified pET11a vector, which has NdeI and XhoI enzyme site.

[b]These primers are designed for the insertion of II^{Mtl} gene from the target genome *Tt* to modified pET32a vector, which has NcoI and XhoI enzyme site.

Table 2. PCR Primers used for mutagenesis.

construct	primers	
*Tt*IIB^{Mtl}	forward 5'	CTCATTGTGTTTGCGTCCGATGCAGGCATGGGT
(C395S)	reverse 3'	ACCCATGCCTGCATCGGACGCAAACACAATGAG
*Tt*IIA^{Mtl}	forward 5'	AAGATAGCTTTGACAAGCCAGTACGAAGAGAAT
(C119A)	reverse 3'	ATTCTCTTCGTACTGGCTTGTCAAAGCTATCTT
*Ec*IIA^{Mtl} Mut$_{I}$	forward 5'	TGGATCGTGAAAAACTGATCACGACTTATCTGGGTGA
(T542I, P543T)	reverse 3'	TCACCCAGATAAGTCGTGATCAGTTTTTCACGATCCA
*Ec*IIA^{Mtl} Mut$_{II}$	forward 5'	CGGTGCCACACGGTGTTTCAGAAGCGAAAGATC
(T556V,V557S)	reverse 3'	GATCTTTCGCTTCTGAAACACCGTGTGGCACCG
*Ec*IIA^{Mtl} Mut$_{III}$	forward 5'	GGTATTGCTGCCCGTAACGACGAGCACATTCAG
(N109D)	reverse 3'	CTGAATGTGCTCGTCGTTACGGGCAGCAATACC

2.2 Protein Expression

2. 2. 1. Protein expression - Luria Bertani medium

Unlabeled protein is used as a ligand partner for titration with isotopically labeled proteins. The expression vectors were transformed into *Escherichia coli* strain BL21 (DE3) (Invitrogen), and the cells were grown in LB medium (Table 3). The cells transformed by the expression vector were cultured at 37°C to an OD_{600} of 0.6–0.8, and the protein overexpression was induced by adding isopropyl-β-D-thiogalactopyranoside (IPTG) to a final concentration of 1 mM, followed by induction for 4 h at 37°C and then harvested by centrifugation. The cell separated on medium was storage on -80 ^{o}C

2. 2. 2. Protein expression - Isotope labeling medium

[^{15}N] / [^{13}C/^{15}N] - labeled proteins are commonly used for increasing the sensitivity of NMR experiments. The expression vectors were transformed into *Escherichia coli* strain BL21(DE3)(Invitrogen) , and the cells were grown in 2ml LB medium for 2 h to inoculate to the M9 minimal media (with $^{15}NH_4Cl$ and/or $^{13}C_6$-glucose as the sole nitrogen or carbon source, respectively) (Table 3). Cells were grown at 37°C until an $OD_{600} \approx$ 0.6–0.8 and induced with 1 mM isopropyl β-D-1-thiogalactopyranoside (IPTG) at 37°C for approximately 8 h or overnight growth at 25°C and harvested by centrifugation.

Table 3. The composition of media

Medium	Composition (per Liter)
LB medium	1 % tryptophan, 0.5 % yeast extract, and 1 % NaCl
M9 minimal medium (^{15}Nitrogen)	10 g K_2HPO_4, 13 g KH_2PO_4, 9 g Na_2HPO_4, 2.4 g K_2PO_4, 1.0g $15NH_4Cl$, 5 g Glucose, 10 mM $MgCl_2$, 0.1 mM Thiamine, 1 x trace elements, 0.2 mM $CaCl_2$, 50 μg/ml carbenicillin.
M9 minimal medium (^{13}Carbon, ^{15}Nitrogen)	10 g K_2HPO_4, 13 g KH_2PO_4, 9 g Na_2HPO_4, 2.4 g K_2PO_4, 1.0 g $^{15}NH_4Cl$, 2.0 g U-$^{13}C_6$ Glucose, 10 mM $MgCl_2$, 0.1 mM Thiamine, 1 x trace elements, 0.2 mM $CaCl_2$, 50 g/ml carbenicillin.

2.3. Protein purification

In this study, proteins are commonly expressed in the modified-pET32 vector that follows common purification step. The purification follows the steps of cell lysis, HisTrap nickel-Sepharose column, exchange to the protease reaction buffer, removal of the His_6-thioredoxin tag, second HisTrap nickel-Sepharose column, the size exclusion chromatography and the final polishing anion or cation exchange chromatography. The other proteins expressed from the pET11a vector has describe individually in the next section.

2.3.1. *Tt*EI

The cell pellet was resuspended in 50 ml (per liter of culture) of 20 mM Tris, pH 7.4, 1mM etlyenediaminetetraacetic acid (EDTA), 1 mM phenylmethylsulfonyl fluoride (PMSF, Sigma, P7626). The suspension was lysed by three passages through Emulsiflex (Avestin, Canada) after homogenizing and centrifuged at 24,000*g* for 20 min at 4ºC. The supernatant was loaded on a HiPrep DEAE column (15ml; GE Healthcare) equilibrated with binding buffer 20 mM Tris-HCl (pH 7.4) and was eluted with a gradient of 1M NaCl. The solutions containing protein were separated by a gel filtration column HiLoad Superdex 200 (GE Healthcare) with 20 mM Tris-HCl (pH 7.4), 200 mM NaCl and finally were purified by Mono Q column (8ml; GE Healthcare). *Tt*EI was analyzed by SDS-polyacrylamide gel electrophoresis to confirm sample mass and sample purity.

2.3.2. *Tt*HPr

The cell containing the *Tt*HPr protein was resuspended in 50 ml of 20 mM Tris, pH 7.4, 200 mM NaCl, and 1 mM PMSF. The suspension was lysed by three passages through Emulsiflex and centrifuged at 24,000 g for 20 min at 4ºC. The

supernatant fraction was filtered and loaded onto a HisTrap nickel-Sepharose column (5ml; GE Healthcare) a 100-ml gradient of imidazole (10–500mM). The fractions containing the protein were confirmed by SDS-PAGE and purified by gel filtration on a Superdex 75 column (GE Healthcare) equilibrated with 20 mM Tris, pH 7.4, 200 mM NaCl. Relevant fractions were exchanged to buffer (20 mM Tris pH 7.4), and finally purified on a monoQ anion exchange column (8ml; GE Healthcare). Final sample was analyzed by SDS-polyacrylamide gel electrophoresis to confirm sample mass and sample purity.

2.3.3. IIA^{Mtl} and IIA^{Mtl} mutants

The cell pellet was resuspended in 50 ml (per liter of culture) of 20 mM Tris, pH 7.4, 200 mM NaCl and 1 mM PMSF (Sigma, P7626). The suspension was lysed by three passages through Emulsiflex (Avestin, Canada) after homogenizing and centrifuged at 24,000*g* for 20 min at 4ºC. The supernatant fraction was filtered and loaded onto a HisTrap nickel-Sepharose column (5ml; GE Healthcare) and the fusion protein was eluted with a 100-ml gradient of imidazole (10–500mM). The protein was then dialyzed against 50 mM Tris, pH 8.0, 4mM β-mercaptoethanol and digested with TEV protease for overnight at room temperature. The cleaved His_6-thioredoxin tag was removed by loading the digested proteins over a nickel-Sepharose column. Relevant fractions were purified by Superdex 75 gel filtration column (GE Healthcare) equilibrated with 20 mM Tris-HCl, pH 7.4, 200 mM NaCl and then on a monoQ anion exchange column (8ml; GE Healthcare) with a 160-ml gradient of 1M NaCl. Final samples were analyzed by SDS-polyacrylamide gel electrophoresis to confirm sample mass and sample purity (Fig. 5).

2.3.4. *Ec*IIB^{Mtl}

Wild type-*Ec*IIB^{Mtl} and *Ec*IIB^{Mtl} (C384S) (375-471) was prepared as above method which is identical to the previous study. [34]

2.3.5. *Tt*IIB^{Mtl}

The cell pellet was resuspended in 50 ml (per liter of culture) of 20 mM Tris, pH 7.4, 200 mM NaCl and 1 mM phenylmethylsulfonyl fluoride (PMSF, Sigma, P7626). The suspension was lysed by three passages through Emulsiflex (Avestin, Canada) after homogenizing and centrifuged at 24,000*g* for 20 min at 4ºC. The supernatant fraction was filtered and loaded onto a HisTrap nickel-Sepharose column (5ml; GE Healthcare) and the fusion protein was eluted with a 100-ml gradient of imidazole (10–500mM). The protein was then dialyzed against 50 mM Tris, pH 8.0, 4mM β-mercaptoethanol and digested with TEV protease for overnight at room temperature. The cleaved His_6-thioredoxin tag was removed by loading the digested proteins over a nickel-Sepharose column. Relevant fractions were purified by Superdex 75 gel filtration column (GE Healthcare) equilibrated with 20 mM Tris-HCl, pH 7.4, 200 mM NaCl and then on a monoS cation exchange column (8ml; GE Healthcare) with a 160-ml gradient of 1M NaCl. Final sample was analyzed by SDS-polyacrylamide gel electrophoresis to confirm sample mass and sample purity

Figure 5. Sample preparation procedure of *Tt*IIA^{Mtl}

Proteins are commonly expressed in the modified-pET32 vector that follows common purification step. The purification follows the step of lysis, supernatant separation, HisTrap nickel-Sepharose column, buffer exchange to the protease reaction buffer, removal of the cleavage His_6-thioredoxin tag by second HisTrap nickel-Sepharose column, size exclusion chromatography and the anion or cation exchange chromatography.

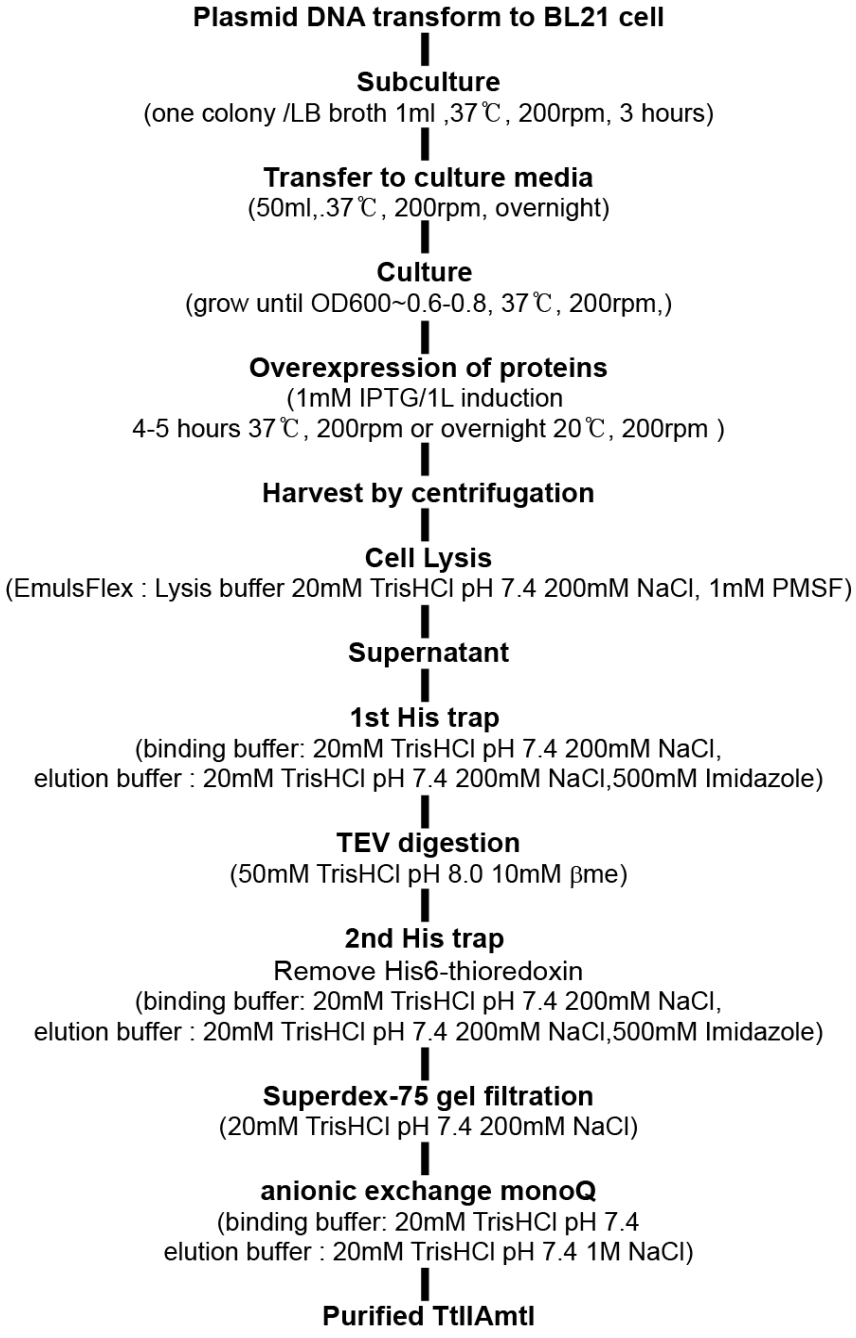
Plasmid DNA transform to BL21 cell
Subculture
(one colony /LB broth 1ml ,37℃, 200rpm, 3 hours)
Transfer to culture media
(50ml,.37℃, 200rpm, overnight)
Culture
(grow until OD600~0.6-0.8, 37℃, 200rpm,)
Overexpression of proteins
(1mM IPTG/1L induction
4-5 hours 37℃, 200rpm or overnight 20℃, 200rpm)
Harvest by centrifugation
Cell Lysis
(EmulsFlex : Lysis buffer 20mM TrisHCl pH 7.4 200mM NaCl, 1mM PMSF)
Supernatant
1st His trap
(binding buffer: 20mM TrisHCl pH 7.4 200mM NaCl,
elution buffer : 20mM TrisHCl pH 7.4 200mM NaCl,500mM Imidazole)
TEV digestion
(50mM TrisHCl pH 8.0 10mM βme)
2nd His trap
Remove His6-thioredoxin
(binding buffer: 20mM TrisHCl pH 7.4 200mM NaCl,
elution buffer : 20mM TrisHCl pH 7.4 200mM NaCl,500mM Imidazole)
Superdex-75 gel filtration
(20mM TrisHCl pH 7.4 200mM NaCl)
anionic exchange monoQ
(binding buffer: 20mM TrisHCl pH 7.4
elution buffer : 20mM TrisHCl pH 7.4 1M NaCl)
Purified TtllAmtl

2.4. Phosphorylation of IIB^{Mtl}

Phosphorylation of *Tt*IIB^{Mtl} or *Ec*IIB^{Mtl} was conducted as follows: 100 μM IIB^{Mtl} was incubated overnight with 5 mM $MgCl_2$, 5 mM phosphoenolpyruvate, 1 μM Enzyme I, 2 μM HPr, and 1 μM IIA^{Mtl} in 20 mM Tris, pH 7.4. *Ec*IIB^{Mtl}(C384S) was phosphorylated at 37°C, and *Tt*IIB^{Mtl}(C395S) was phosphorylated at 65°C. The phosphorylation reaction was monitored by native gel electrophoresis, and purified by monoQ anion exchange chromatography (GE Healthcare). Phosphorylation was confirmed by mass spectrometry and 2-D heteronuclear single quantum correlation (HSQC) NMR spectra. Purified proteins were finally concentrated in 20 mM Tris, pH 7.4.

2.5. NMR spectroscopy and structure calculation

2.5.1. Backbone structure determination

NMR samples contained 1mM [U-$^{15}N/^{13}C$]- *Tt*IIA^{Mtl} (C119A) and [U-$^{15}N/^{13}C$]-phospho-*Tt*IIB^{Mtl} (C395S) in 20mM Tris, pH 7.4 and 90% H_2O /10% D_2O. NMR spectra were collected at 298K on Bruker AVANCE 700MHz and 900MHz spectrometers equipped with either a *z-shielded* gradient triple resonance cryoprobe. Sequential assignments of ^{13}C, ^{15}N-labeled *Tt*IIA^{Mtl} and phospho-*Tt*IIB^{Mtl}(C395S) were performed using 2D ^{15}N-HSQC spectrum and 3-D triple resonance through-bond scalar correlation experiments such as experiments (3D HNCO, HNCACO, HNCA, HN(CO)CA, HNCACB, CBCA(CO)NH. NMR Spectra were processed using the NMRPipe[40] program and analyzed using the PIPP/CAPP/STAPP[41] and NMRView[42] programs. Overall secondary structure and the backbone dihedral torsion angles (φ/ψ) were derived from TALOS+[43] based on combined H_N, ^{15}N, Cα, Cβ and CO backbone chemical shifts.

2.5.2. NMR Titration

For NMR titration measurement, experiments were acquired on a Bruker 600 MHz z-shielded gradient triple resonance cryoprobe at 298K. 0.3 mM ^{15}N-labeled samples were titrated with unlabeled partner proteins up to a 1:7.2 molar ratio. Measured ^{1}H and ^{15}N chemical shift changes were weighted using the equation $\Delta\delta_{HN} = [(\Delta\delta_H^2 + 0.04\ \Delta\delta_N{}^2)/2]^{1/2}$. The titration data were fit to a simple equilibrium binding model to yield the equilibrium dissociation constant (K_D) using the equation, $\Delta\delta_{obs} = \Delta\delta_{max}\frac{\{([A]+[B]+K_D)-[([A]+[B]+K_D)^2-(4[A][B])]^{1/2}\}}{2[A]}$, where $\Delta\delta_{obs}$ is the observed chemical shift change, $\Delta\delta_{max}$ is the maximum chemical shift change, and [A] and [B] are the total protein concentrations of the titrate and the titrant, respectively[44].

2.5.3. Residual Dipolar Coupling (RDC)

$^{1}D_{NH}$ RDCs were measured by taking the difference in $^{1}J_{NH}$ scalar couplings in aligned and isotropic media[45, 46] at 25 °C. The alignment media employed were phage *pf1*[47](ASLA Biotech), 5% $C_{12}E_5$, polyethylene glycol (PEG)/*n*-hexanol (Fluka)[48], and axially stretched neutral polyacrylamide gels (5.5% (w/v) polyacrylamide)[49]. Singular value decomposition (SVD) analysis[49] of RDCs was carried out using Xplor-NIH.[51]

2.6 ITC

ITC was performed using an iTC_{200} calorimeter (GE Healthcare). 0.5 mM *Tt*IIA^{Mtl} or *Ec*IIA^{Mtl} were placed in the cell and titrated with 5 mM phospho-*Tt*IIB^{Mtl}(C395S) in the syringe at 25°C for wild-type and mutant proteins in 20 mM TrisHCl, pH 7.4. Titrations was employed as twenty consecutive 2 µL aliquots of phospho-

*Tt*IIB^{Mtl}(C395S) into the cell containing IIA^{Mtl} with intervals of 180 sec. Analysis of the data was performed using the Origin software provided with the instrument.

3. Results

In this study, interaction between *Tt*IIA^{Mtl} and *Tt*IIB^{Mtl} has been examined by using NMR spectroscopy and ITC. Individual domains of *T. tengcongensis* and *E. coli* adopt the same backbone folds, but separate domains exhibit a 28-times higher affinity than the linked ones. The key binding determinants are identified, and the biological significances are discussed.

3. 1. Structure of *Tt*IIA^{Mtl}, phospho-*Tt*IIB^{Mtl}

The resonance assignment of the macromolecule is a prerequisite for protein-detected methods, structural and dynamic studies. Structural studies suggest that high affinity interactions arise as the sum of many close range noncovalent interactions, and therefore, the complementarity between molecules is essential for the formation of high affinity molecular recognition. To study the structure of the domains, we cloned *Tt*IIA^{Mtl}(1–146) and *Tt*IIB^{Mtl}(386–477) based on the sequence alignment with the homologous *Ec*IIA^{Mtl}(490–637) and *Ec*IIB^{Mtl}(375–471).

3.1.1. Resonance assignment of *Tt*IIA^{Mtl}

*Tt*IIA^{Mtl} consists of 146 amino acid residues with molecular weight of 16.4 kDa. The ^{1}H, ^{15}N and ^{13}C assignment obtained for *Tt*IIA^{Mtl} are listed in Table 1. Backbone assignments for amide resonances were obtained for 133 residues out of 141 residues (94%), excluding four proline residues and the N-terminal methionine.[38] The 2D ^{1}H-^{15}N HSQC spectrum of *Tt*IIA^{Mtl} shows well dispersed amide resonances (Fig. 6). The assignments are annotated with residue types and numbers in Figure 1. Six of the nine missing assignments are due to the absence of the corresponding

amide resonances, and the remaining three residues were (Gly-105, Asp-106, Glu-107) unassigned because of severe spectral overlap. In summary, 97% of C_α, 96% of C_β and 95% of CO were assigned and listed in Table 4.

Secondary structural information of *Tt*IIA^{Mtl} was calculated based on the $^{1}H_N$, ^{15}N, C_α, C_β and CO chemical shift by using TALOS + program[43] based on the artificial neural network algorithm. The results of secondary structure are presented in Figure 7. The height of the bars reflects the probability of the secondary structure prediction. The secondary structure prediction showed that *Tt*IIA^{Mtl} is comprised of six β strands and six α-helices. Residue Ile-11~Leu-13 (β1), Thr-53~Tyr-55 (β2), Val-60~Ile-62 (β3), Ile-73~Tyr-83 (β4), Gly-86~Asp-88 (β5) and Arg-94~Gly-103 (β6) constitute the β strands, and Lys-20~Glu-33 (α1), Lys-39~Glu-50 (α2), Ser-67~Lys-71 (α3), Glu-107~Ala-119 (α4), Tyr-121~Lys-130 (α5) and Pro-134~Lys-143 (α6) constitute the α-helices. *Ec*IIA^{Mtl} is composed of a central five-stranded beta sheet, flanked by five alpha helices. Overall secondary structures of *Ec*IIA^{Mtl} and *Tt*IIA^{Mtl} are in good agreement, with a slight difference in the distribution of secondary structure elements. The β4 region of *Ec*IIA^{Mtl} is segmented into β4 and β5 of *Tt*IIA^{Mtl}.

The results of predicted backbone torsion angles (φ, ψ) are presented in Ramachandran plot (Fig. 7), 129 residues are in most favorable regions and remaining three resonances also belong to allowed regions and did not showed any outlier in the plot. Notwithstanding, the data suggest that *Ec*IIA^{Mtl} and *Tt*IIA^{Mtl} would share a common local and global structures.

RDCs of backbone amide groups of *Tt*IIA^{Mtl} are measured to examine whether they adopted the same backbone folds as their homologues in *E. coli*. RDCs were measured using 11 mg/ml of phage *pf1* as an alignment media[46, 48]. Comparison of

observed and calculated $^{1}D_{NH}$ RDCs using the solution structures of *Ec*IIA^{Mtl} (PDB code 2FEW chain A), showed a good fitting with RDC R-factors of 21.5% (Fig. 8). This R-factor is compatible to the terms of R-factor in crystallography the value 0.2 is corresponds to resolution of 2.5 Å. The results indicate that backbone folds of individual domains of *T. tengcongensis* are largely the same as those of *E. coli*.

Figure 6. $^{1}H-^{15}N$ HSQC spectra of $^{13}C/^{15}N$-labelled *Tt*IIA^{mtl} in 20mM TrisHCl pH 7.4, 298K.

Assignments are annotated by residue name and number. An expansion of the boxed region is provided in the upper left corner.

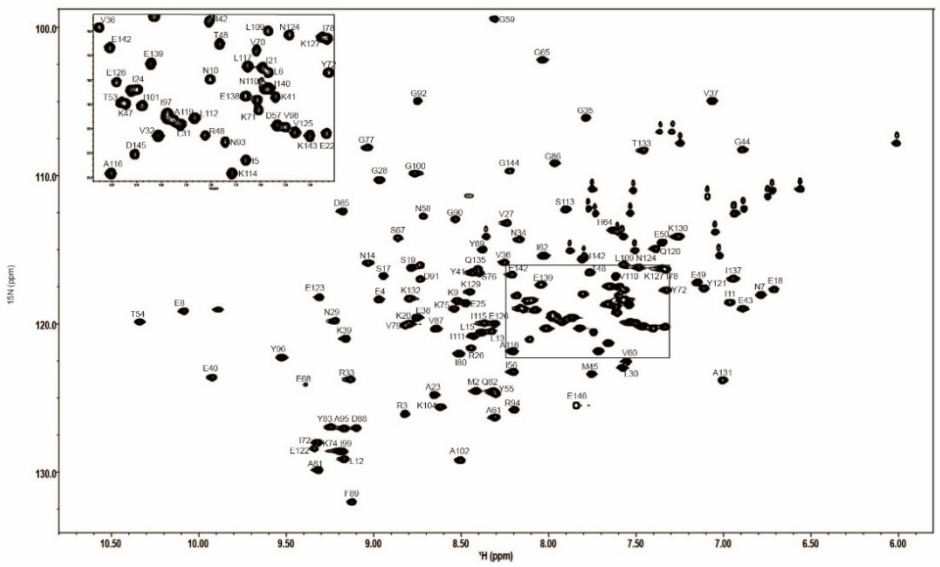
15N (ppm)
100.0
110.0
120.0
130.0
10.50
10.00
9.50
9.00
8.50
8.00
7.50
7.00
6.50
6.00
1H (ppm)

Figure 7. Predicted secondary structure (upper panel) and the backbone derived Ramachandran plot of *Tt*IIA^{Mtl} (lower panel).

Predicted secondary structure (blue positive bar, beta-sheet; red negative bar, helix) for all residues are shown in the lower panel. The height of the bars reflects the probability of the neural network secondary structure prediction, and schematic representations of secondary structure are displayed above the prediction scores (upper panel). Backbone torsion angles (ϕ, ψ) were predicted using TALOS+ with backbone chemical shifts and plotted upon the Ramachandran plot (lower panel).

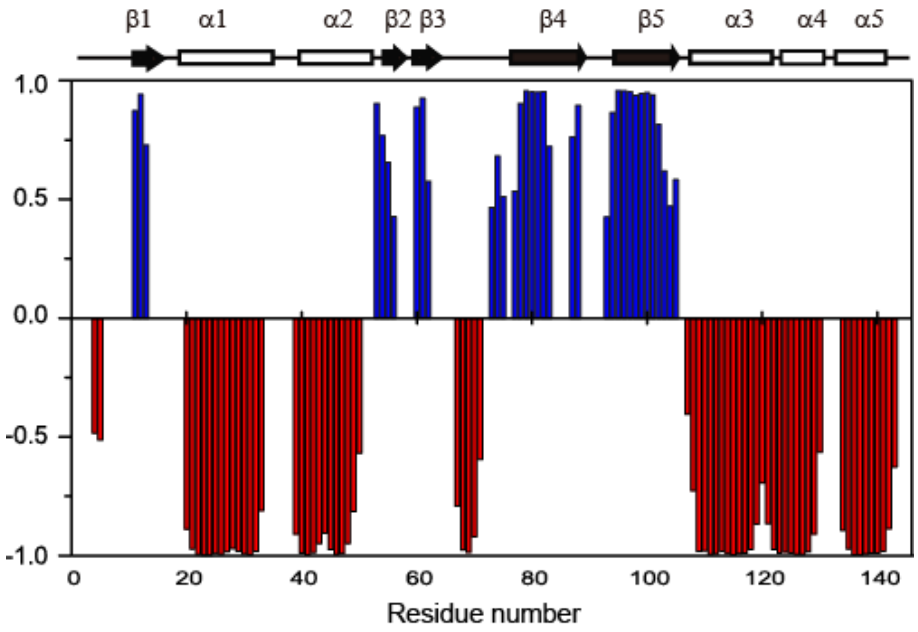
β1 α1 α2 β2 β3 β4 β5 α3 α4 α5
1.0
0.5
0.0
-0.5
-1.0
0 20 40 60 80 100 120 140
Residue number

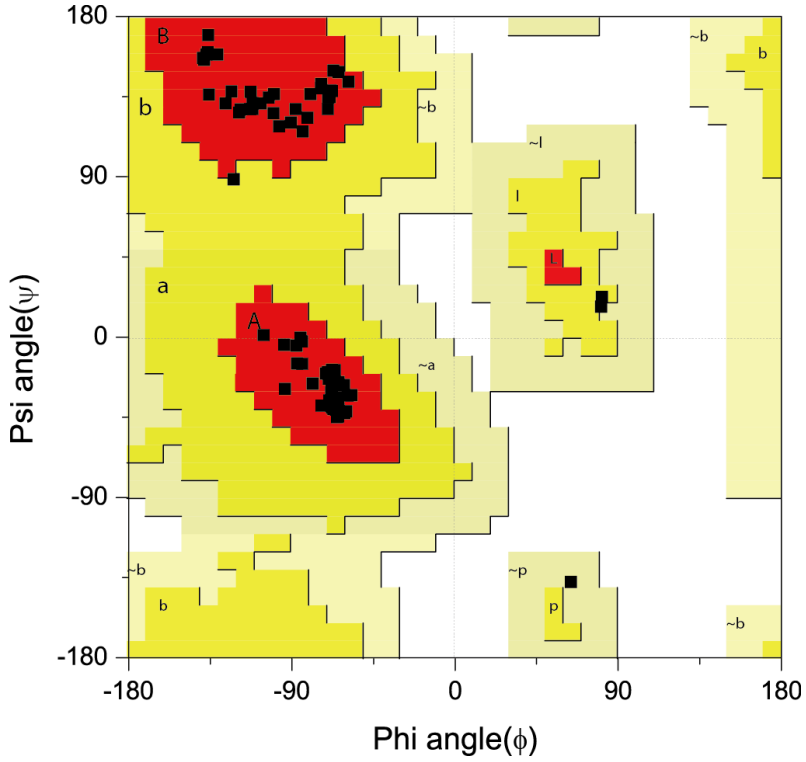
180
90
0
-90
-180
-180 -90 0 90 180
Psi angle(ψ)
Phi angle(ϕ)
B
b
~b
~l
l
L
a
A
~a
~p
p
~b
b

Figure 8. RDC analysis of *Tt*IIA^{Mtl}.

Comparison of observed and calculated $^{1}D_{NH}$ RDCs obtained by SVD with the structures of *Ec*IIA^{Mtl} (PDB code 2FEW, chain A) is shown. The RDCs were measured in an alignment medium of 11 mg/ml phage *pf1*. The values of RDC R-factors and the correlation coefficients (*r*) are described. The magnitude of the principal component of the tensor (D_a^{NH}), and the rhombicity (η) are as follows: −6.1 and 0.49

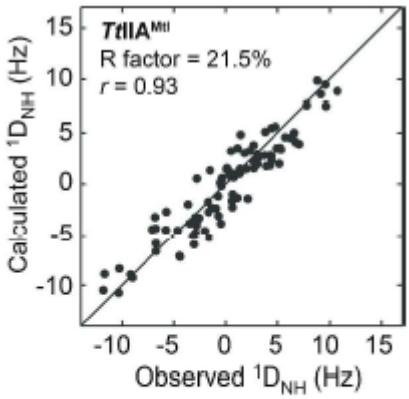
TtIIA^MII
R factor = 21.5%
r = 0.93
Calculated 1D_NH (Hz)
Observed 1D_NH (Hz)
15
10
5
0
-5
-10
-10
-5
0
5
10
15

Table 4. Backbone HN, N, C_{α}, C_{β}, CO chemical shifts of *Tt*IIA^{Mtl} (unit: ppm).

Residue	HN	N	CA	CB	CO
1 MET			54.97	33.56	175.51
2 ASP	8.414	124.52	54.97	41.77	177.69
3 ARG	8.823	126.08	56.74	29.69	177.93
4 GLU	8.970	118.35	58.64	29.30	178.72
5 ILE	7.659	121.30	63.10	39.08	174.03
6 LEU	7.569	117.77	54.18	44.32	
7 ASN	6.790	118.05	51.91	40.78	
8 GLU	10.084	119.14	60.66	28.94	177.20
9 LYS	8.523	118.45	57.61	31.16	176.99
10 ASN	7.804	118.00	51.95	39.13	173.11
11 ILE	6.965	118.55	60.26	40.30	174.04
12 LEU	9.168	129.12	53.07	45.15	174.51
13 LEU	8.324	120.49	53.74	43.79	177.05
14 ASN	9.032	115.90	54.18	37.82	174.74
15 LEU	8.382	120.57	56.41	42.32	175.32
16 PRO			61.80	31.86	176.90
17 SER	8.944	116.77	62.50	63.79	171.94
18 GLU	6.711	117.67	53.38	29.86	174.25
19 SER	8.786	116.22	58.45	65.02	173.95
20 LYS	8.801	119.98	59.71	30.28	177.16
21 ILE	7.590	117.51	63.48	36.44	177.67
22 GLU	7.334	120.20	59.38	28.92	179.29
23 ALA	8.656	124.80	55.25	19.03	179.73
24 ILE	8.099	118.41	66.45	37.69	178.04
25 GLU	8.473	118.60	60.28	28.89	177.87
26 ARG	8.443	121.62	60.28	29.75	180.60
27 VAL	8.238	113.19	65.52	31.37	178.40
28 GLY	8.968	110.30	48.40		174.61
29 ASN	9.219	119.79	56.36	38.05	178.01
30 LEU	7.574	122.96	57.62	41.75	178.73
31 LEU	7.925	119.86	59.19	42.96	179.56
32 VAL	8.013	120.31	64.88	32.31	180.95
33 ARG	9.132	123.74	59.42	29.70	178.37
34 ASN	8.166	114.30	52.49	37.18	175.00

Residue	HN	N	CA	CB	CO
35 GLY	7.788	106.10	46.10		174.31
36 VAL	8.251	115.85	61.48	38.86	176.63
37 GLU	7.064	104.96	57.30	36.27	175.46
38 GLU	8.754	119.57	55.06	31.15	178.52
39 LYS	9.158	121.00	60.11	32.37	
40 GLU	9.923	123.62	60.77	27.07	177.86
41 TYR	8.436	116.54	62.59	40.02	176.96
42 ILE	7.809	115.64	65.66	37.59	178.35
43 GLU	6.890	118.97	59.06	28.79	178.42
44 GLY	6.893	108.24	45.60		176.17
45 MET	7.755	123.39	58.39	34.93	178.46
46 LYS	7.540	118.74	60.46	31.95	178.74
47 LYS	8.148	118.97	58.88	32.26	179.17
48 ARG	7.824	120.30	58.33	29.46	177.30
49 GLU	7.147	117.20	57.39	29.37	176.83
50 GLU	7.348	114.51	57.84	29.69	177.24
51 ASP	7.533	119.88	56.64	42.06	176.10
52 ILE	8.122	118.46	60.52	40.87	173.47
53 THR	8.148	118.97	62.24	69.10	174.35
54 THR	10.338	119.87	62.48	68.53	175.96
55 TYR	8.301	124.76	60.14	39.18	175.94
56 ILE	8.201	123.24	61.01		175.42
57 GLY			43.98		172.47
58 ASN	8.717	112.73	53.85	37.38	174.87
59 GLY	8.308	99.44	46.83		174.86
60 VAL	7.554	122.54	61.04	33.72	172.89
61 ALA	8.306	126.32	50.03	23.51	175.73
62 ILE	8.029	115.40	57.31	39.09	171.72
63 PRO			64.65	32.68	173.84
64 HIS	7.632	113.68	56.09	30.28	171.28
65 GLY	8.036	102.18	42.97		
66 VAL			59.92	35.14	176.12
67 SER	8.863	114.21	60.20	61.92	178.38
68 GLU	9.386	124.12	59.15	29.30	176.92
69 TYR	8.376	114.98	60.73	37.40	177.22
70 VAL	7.616	116.80	64.89	30.88	178.23

Residue	HN	N	CA	CB	CO
71 LYS	7.608	119.27	57.51	30.80	176.43
72 TYR	7.324	117.72	57.53	38.78	173.78
73 ILE	9.321	128.01	61.42	33.69	174.04
74 LYS	9.185	128.60	58.14	32.66	177.02
75 LYS	8.540	118.99	55.30	35.49	172.90
76 SER	8.398	116.59	59.36	64.05	177.81
77 GLY	9.035	108.10	45.72		170.35
78 ILE	7.347	116.24	59.32	42.35	173.78
79 VAL	8.817	120.13	58.76	35.29	174.70
80 ILE	8.511	122.01	60.71	41.50	172.03
81 ALA	9.315	129.86	50.16	22.28	174.03
82 GLN	8.313	124.55	54.54	33.96	172.12
83 TYR	9.245	126.95		40.12	175.47
84 PRO			65.90	32.45	177.22
85 ASP	9.175	112.41	54.22	41.90	178.70
86 GLY	7.965	109.16	44.57		171.54
87 VAL	8.644	120.32	60.87	35.41	175.59
88 ASP	9.097	127.03	54.54	40.16	175.23
89 PHE	9.123	132.01	59.02	40.34	176.63
90 GLY	8.533	112.94	44.49		173.10
91 ASP	8.734	116.98	55.69	39.96	175.34
92 GLY	8.750	104.96	45.25		174.42
93 ASN	7.742	120.57	52.24	37.60	173.09
94 ARG	8.194	125.80	54.83	31.70	173.92
95 ALA	9.168	127.06	50.25	21.63	175.42
96 TYR	9.527	122.27	58.86	41.09	174.05
97 ILE	7.977	119.45	57.71	38.30	176.29
98 VAL	7.500	119.93	62.67	38.38	175.09
99 ILE	9.183	128.60	59.48	39.34	175.93
100 GLY	8.765	109.86	44.80		173.11
101 ILE	8.078	119.05	59.65	42.85	175.01
102 ALA	8.505	129.20	52.15	22.33	173.46
103 GLY			43.89		170.96
104 LYS	8.621	125.62	55.57	33.19	177.26
105 GLY					
106 ASP					

Residue	HN	N	CA	CB	CO
107 GLU					
108 HIS			60.70	31.34	175.86
109 LEU	7.570	115.98	57.42	41.04	179.89
110 ASN	7.597	118.08	56.32	38.17	177.72
111 ILE	8.430	120.84	65.87	38.41	177.46
112 LEU	7.866	119.58	59.05	41.72	178.95
113 SER	7.904	112.28	61.55	62.77	176.53
114 LYS	7.717	121.85	59.15	32.27	179.69
115 ILE	8.368	119.95	63.17	35.92	177.43
116 ALA	8.203	121.85	55.49	17.68	179.95
117 LEU	7.652	117.46	57.79	41.69	179.79
118 THR	7.766	116.53	67.05	68.67	176.29
119 ALA	7.974	119.49	53.01	18.59	176.01
120 GLN	7.385	114.93	57.05	28.56	175.20
121 TYR	7.111	117.61	61.52	28.56	176.28
122 GLU	9.337	128.42	60.53	29.38	178.05
123 GLU	9.309	118.21	59.34		179.09
124 ASN	7.484	116.18	55.37	37.87	177.44
125 VAL	7.461	120.16	67.05	31.26	178.02
126 GLU	8.309	120.00	59.44	28.88	178.89
127 LYS	7.334	116.32	59.79	32.55	178.89
128 LEU	7.950	119.69	58.10	42.16	178.64
129 LYS	8.450	117.84	60.03	32.61	176.77
130 LYS	7.258	114.11	55.60	33.40	176.58
131 ALA	7.005	123.80	53.27	19.53	177.92
132 LYS	8.796	118.29	55.97	34.92	176.63
133 THR	7.456	108.30	57.94	70.49	173.13
134 PRO			65.32	32.56	177.81
135 GLN	8.403	116.28	59.77	27.12	177.81
136 GLU	7.613	118.86	59.25	30.80	178.77
137 ILE	6.945	116.95	63.86	36.62	176.70
138 ILE	7.661	118.67	66.34	37.85	176.97
139 GLU	8.043	117.35	59.39	29.52	179.27
140 ILE	7.571	118.37	64.25	38.01	178.30
141 LEU			57.42	41.68	
142 GLU	8.212	116.73	60.64	30.12	177.18

Residue	HN	N	CA	CB	CO
143 LYS	7.400	120.31	57.43	32.42	177.45
144 GLY	8.220	109.67	45.67	57.63	173.73
145 ASP	8.108	121.04	54.16	41.38	175.25
146 GLU	7.843	125.51	58.23	31.08	

3.1.2. Resonance assignment of phospho-*Tt*IIB^{Mtl} (C395S)

NMR spectra of *Tt*IIB^{Mtl}

Since the phosphoryl transfer reaction between active site His-64 of *Tt*IIA^{Mtl} and Cys-395 of *Tt*IIB^{Mtl} took place in a reversible manner, but the phosphoryl groups on histidine and cysteine were labile and slowly lost to buffer by acid- or base-catalyzed dephosphorylation reactions. When the active site Cys-395 of *Tt*IIB^{Mtl} was mutated to serine, *Tt*IIB^{Mtl}(C395S) could be permanently phosphorylated as a stable form. Phospho-*Tt*IIB^{Mtl}(C395S) was stable, and did not engage in further phosphoryl transfer reactions, which was also observed in the phospho-*Ec*IIB^{Mtl}(C384S) mutant of *E. coli*. ^{1}H-^{15}N HSQC spectra (Fig. 9) shows well-isolated backbone amide resonances of phospho-*Tt*IIB^{Mtl}(C395S), indicating a compact fold. Furthermore, in comparison with unphospho-*Tt*IIB^{Mtl}, line broadened cross peak at the active site loop was shown for phospho-*Tt*IIB^{Mtl} (Fig. 10).

NMR assignment of phospho-*Tt*IIB^{Mtl} (C395S)

Backbone assignment of phospho-*Tt*IIB^{Mtl} (C395S), consists of 92 amino acid residues with molecular weight of 10.6 kDa, has carried out using a suite of heteronuclear triple resonance NMR spectroscopy. The ^{1}H, ^{15}N and ^{13}C assignment obtained for phospho-*Tt*IIB^{Mtl} (C395S) are listed in Table 5. Backbone assignments for amide resonances were obtained for 82 residues out of 89 residues (92%), excluding three proline residues and Phe-460 to Val-466, which is predicted to flexible loop by sequential alignment between known phospho-*Ec*IIB^{Mtl} (C384S). Absence of the amide peak is probably due to a process involving exchange with the solvent and conformational changes in the flexible loop. The assignments are

annotated with residue types and numbers in Figure 9.

Secondary structural information of phospho-*Tt*IIB^{Mtl}(C395S) was calculated based on the $^{1}H_{N}$, ^{15}N, C_{α}, C_{β} and CO chemical shift by using TALOS+ program[43] based on the artificial neural network algorithm. The height of the bars reflects the probability of the secondary structure prediction (Fig. 11). The secondary structure prediction showed that phospho-*Tt*IIB^{Mtl} (C395S) is comprised of four β strands and three α-helices. Residue Leu-390~Ser-395 (β1), Phe-418~Ala-426 (β2), Val-436~Thr-439 (β3) and Lys-455~Val-459 (β4) constitute the β strands, and Ser-401~Glu-415 (α1), Glu-441~Val-450 (α2) and Phe-462~Leu-475 (α3) constitute the α-helices. phospho-*Ec*IIB^{Mtl} is composed of a central four-stranded beta sheet, flanked by three alpha helices. Overall secondary structures of phospho-*Ec*IIB^{Mtl} and phospho-*Tt*IIB^{Mtl} are in good agreement that suggests phospho-*Ec*IIB^{Mtl} and phospho-*Tt*IIB^{Mtl} would share a common backbone scaffold.

The results of backbone torsion angles (φ, ψ) are presented in Figure 11, 73 residues are in most favorable regions and six residues are in allowed region, and three residues are in generously allowed regions and did not showed any outlier in the plot. Notwithstanding, the data suggest that phospho-*Ec*IIB^{Mtl} and phospho-*Tt*IIB^{Mtl} (C395S) would share a common local and global structures.

RDCs of backbone amide groups of unphospho-*Tt*IIB^{Mtl}, and phospho-*Tt*IIB^{Mtl} (C395S) were measured to examine whether they adopted the same backbone folds as their homologues in *E. coli*. RDCs were measured using 11 mg/ml of phage pf1 and 500 mM of NaCl as an alignment media.[46] For unphospho-*Tt*IIB^{Mtl} and phospho-*Tt*IIB^{Mtl}(C395S), NaCl was employed to prevent nonspecific interactions between *Tt*IIB^{Mtl} and phage *pf1*.[48] Comparison of observed and calculated $^{1}D_{NH}$ RDCs using the solution structures of phospho-*Ec*IIB^{Mtl}(C384S) (PDB code 2FEW chain B) showed a good fitting with RDC R-factors of 20.9% for phospho-

*Tt*IIB^{Mtl}(C395S) (Fig. 12), For unphospho-*Tt*IIB^{Mtl}, calculation was performed except in case of undetectable cross peaks that belong to the flexible active site loop (residues 395-402; CDAGMGSS), which experiences line broadening. Unphosphorylated *Ec*IIB^{Mtl} (PDB code 1VKR) showed a good fitting with RDC R-factors of 20.7% for *Tt*IIB^{Mtl} (Fig. 12). The results indicate that backbone folds of individual domains of *T. tengcongensis* are largely the same as those of *E. col*. within resolution of 2.5Å.

Figure 9. $^{1}H-^{15}N$ HSQC spectra of $^{13}C/^{15}N$-labelled phospho-*Tt*IIB^{mtl} in 20mM TrisHCl pH 7.4, 298K.

Assignments are annotated by residue name and number. An expansion of the boxed region is provided in the upper left corner.

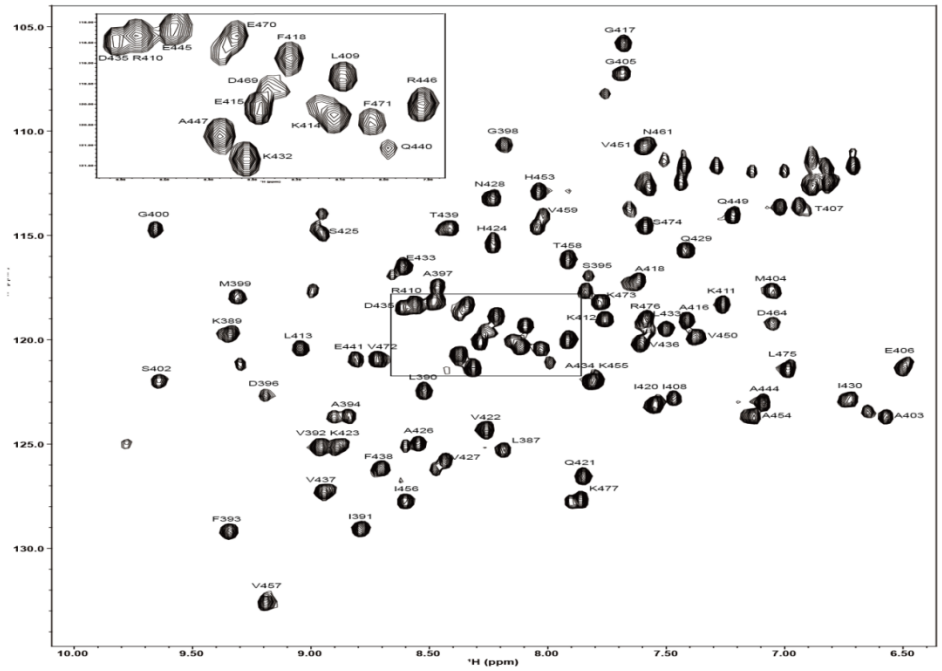
105.0
110.0
115.0
120.0
125.0
130.0
10.00
9.50
9.00
8.50
8.00
7.50
7.00
6.50
¹H (ppm)
E470
F418
L409
D469
R446
E415
F471
A447
K414
Q440
K432
D435 R410
E445
G417
G405
G398
N461
V451
H453
N428
V459
T407
Q449
G400
S425
T439
H424
S474
Q429
T458
E433
S395
A418
A397
M404
M399
R410
K473
K411
D439
R476
A416
D464
K389
K412
L433
V450
V436
L413
E441
V472
L475
E406
S402
L390
A434
K455
D396
I420
I408
A444
I430
A394
A454
A403
V422
V392
K423
A426
L387
F438
V427
Q421
V437
K477
I456
F393
I391
V467

Figure 10. Superimposed $^{1}H,^{15}N$–HSQC spectra of ^{15}N labelled unphospho-*Tt*IIB^{Mtl} (black circle) and phospho-*Tt*IIB^{Mtl} (red empty circle).

Phospho- *Tt*IIB^{Mtl} shows additional cross peaks at the active site loop, assigned residues name and the number has annotated on the spectrum.

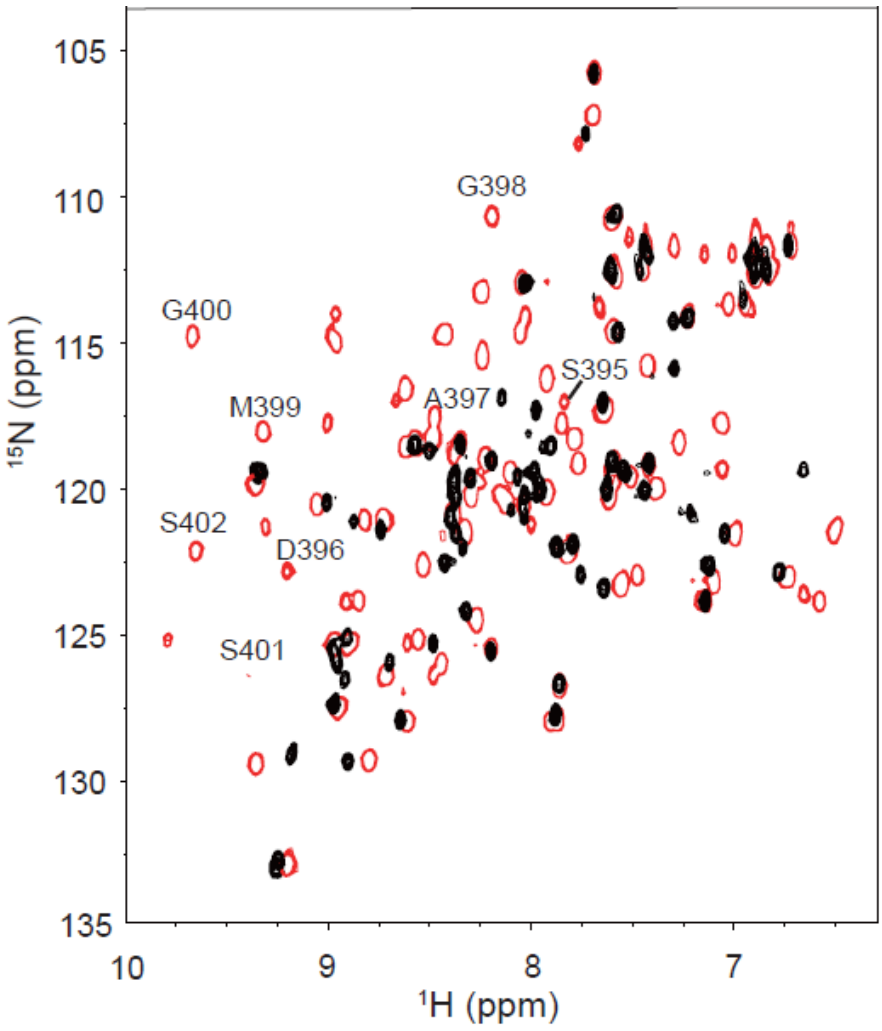
105
110
115
120
125
130
135
^{15}N (ppm)
10
9
8
7
^{1}H (ppm)
G398
G400
S395
A397
M399
S402
D396
S401

Figure 11. Predicted secondary structure (upper panel) and the backbone derived Ramachandran plot of phospho-*Tt*IIB^{Mtl} (lower panel).

Predicted secondary structure[46] (blue positive bar, beta-sheet; red negative bar, helix) for all residues are shown in the lower panel. The height of the bars reflects the probability of the neural network secondary structure prediction, and schematic representations of secondary structure are displayed above the prediction scores (upper panel). Backbone torsion angles (ϕ, ψ) were predicted using TALOS+ with backbone chemical shifts and plotted upon the Ramachandran plot (lower panel)

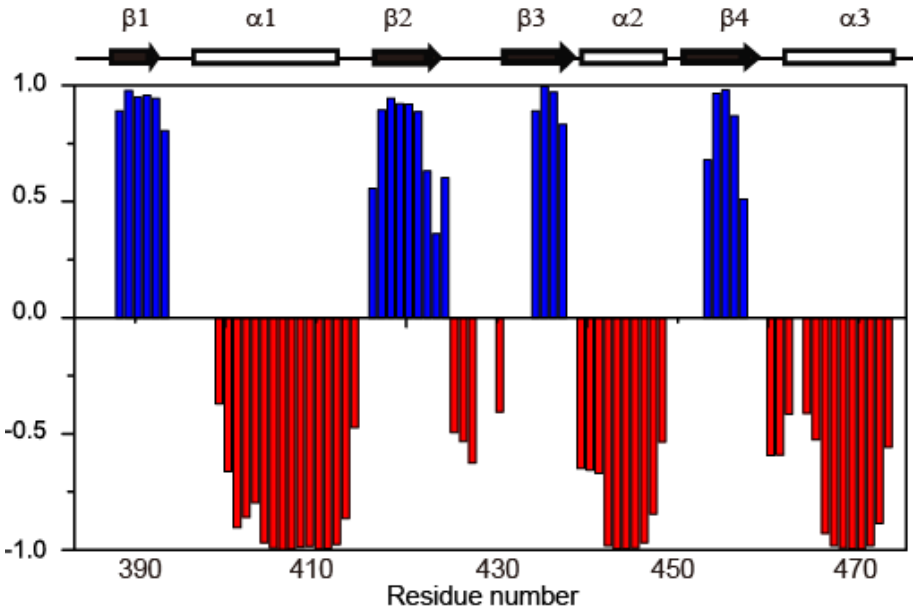
β1
α1
β2
β3
α2
β4
α3
1.0
0.5
0.0
-0.5
-1.0
390
410
430
450
470
Residue number

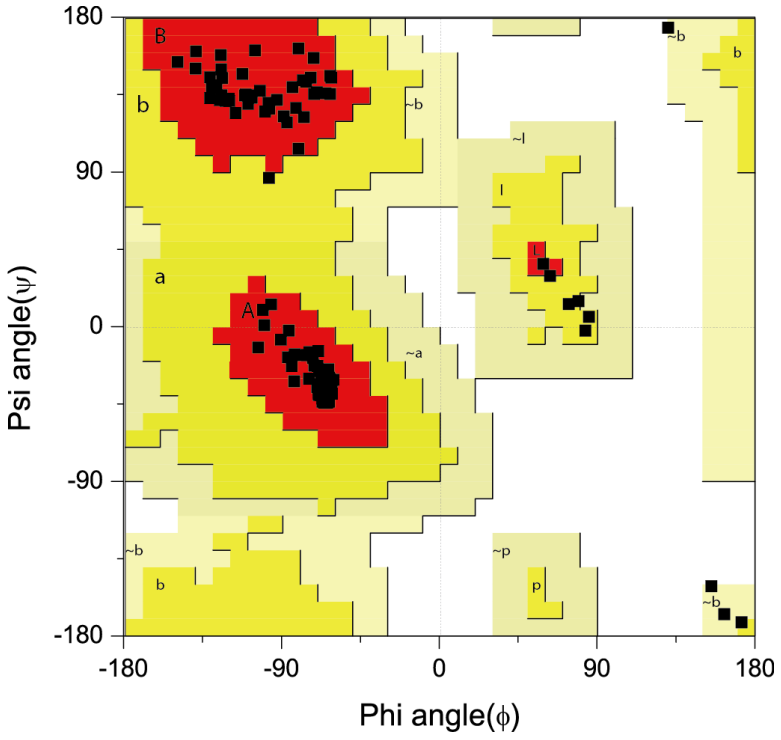
180
90
0
-90
-180
-180
-90
0
90
180
Psi angle(ψ)
Phi angle(ϕ)
B
b
a
A
~b
~l
l
~a
~p
p

Figure 12. RDC analysis of unphospho-*Tt*IIB^{Mtl}(upper panel), phospho-*Tt*IIB^{Mtl}(C395S) (lower panel).

Comparison of observed and calculated $^{1}D_{NH}$ RDCs obtained by SVD with the structures of unphosphorylated-*Ec*IIB^{Mtl} (PDB code 1VKR) and phospho- *Ec*IIB^{Mtl} (PDB code 1VRV) is shown. The RDCs were measured in an alignment medium of 11 mg/ml phage *pf1*with 500mM NaCl. The values of RDC R-factors and the correlation coefficients (*r*) are described. The magnitude of the principal component of the tensor (D_a^{NH}), and the rhombicity (η) are as follows: 7.9 and 0.25 for *Tt*IIB^{Mtl}, and 5.8 and 0.28 for phospho-*Tt*IIB^{Mtl}(C395S).

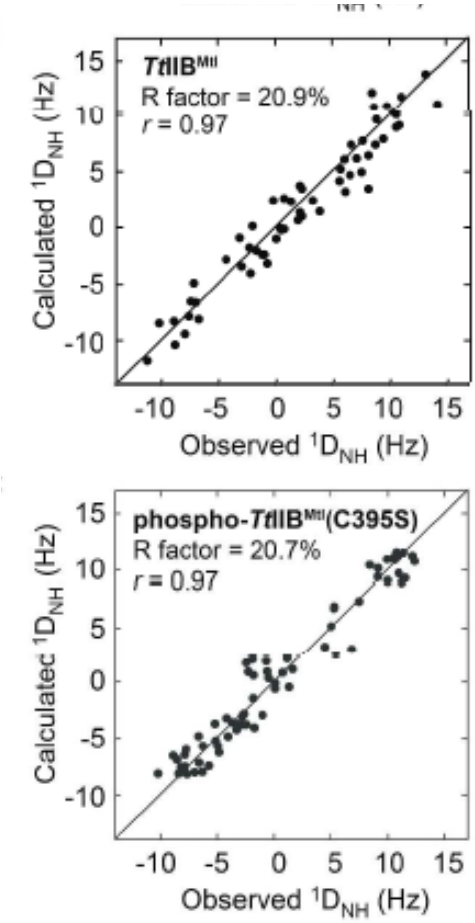
TtIIB^MII
R factor = 20.9%
r = 0.97
Calculated 1DNH (Hz)
Observed 1DNH (Hz)
phospho-TtIIB^MII(C395S)
R factor = 20.7%
r = 0.97
Calculatec 1DNH (Hz)
Observed 1DNH (Hz)

Table 5. Backbone HN, N, Cα, Cβ, CO chemical shifts of phospho-*Tt*IIB^{Mtl} (unit: ppm)

Residue	HN	N	CA	CB	CO
1 THR	7.835	112.5	60.8	70.3	174.29
2 LEU	8.21	125.21	53.25	41.95	175.09
3 PRO			62.83	32.76	
4 LYS	9.405	119.8	57	33.78	173.92
5LEU	8.573	122.48	55.49	43.13	174.25
6 ILE	8.813	129.04	59.57	40.17	173.22
7 VAL	9.003	125.23	59.55	35.64	174.64
8 PHE	9.383	129.24	57.1	42.1	177.09
9 ALA	8.894	123.76	50.25	22.94	172.78
10 SER	7.879	117.78	55.88	68.37	176.73
11 ASP	9.227	122.68	58.77	41.78	178.63
12 ALA	8.486	117.42	52.19	20.01	174.81
13 GLY	8.217	110.66	46.59		176.52
14 MET	9.357	118.01	54.59	34.89	175.77
15 GLY	9.72	114.78	46.25		175.52
16 SER	9.425	126.84	62.03	63.04	176.01
17 SER	9.718	122.09	61.24	62.38	179.66
18 ALA	6.701	123.49	53.8	17.26	178.8
19 MET	7.106	117.71	57.55	31.58	173.1
20 GLY	7.733	107.26	47.91		176.95
21 GLU	6.541	121.41	58.46	28.68	176.47
22 THR	7.06	113.68	66.29	68.77	178.43
23 ILE	7.515	122.85	64.96	38.1	181.37
24 ARG	8.135	119.42	57.86	40.18	178.46
25 ARG	8.614	118.29	60.83	29.99	178.77
26 LYS	7.3	118.37	59.9	32.39	178.78
27 LYS	7.804	119.05	59.66	33.6	181.46
28 LEU	9.09	120.38	58.36	41.34	177.52
29 LYS	8.148	120.36	59.37	31.93	176.43
30 GLU	8.321	120.13	59.04	29.42	174.19

Residue	HN	N	CA	CB	CO
31 ALA	7.466	119.18	52	19.97	174.94
32 GLY	7.723	105.79	45.52		174.86
33 PHE	8.264	118.94	57.14	42.05	174.14
34 ASP	9.143	124.47	53.46	41.41	175.14
35 ILE	7.544	123.15	60.45	42.52	176.12
36 GLN	7.912	126.58	57.12	29.77	173.03
37 VAL	8.26	124.24	59.91	34.33	182.42
38 LYS	8.935	125.19	55.03	38.21	174.47
39 HIS	8.256	115.12	63.14	30.91	176.06
40 SER	9.005	114.99	58.14	67.58	174.59
41 ALA	8.579	124.94	52.12	19.02	177.02
42 VAL	8.504	126.2	65.62	31.59	177.62
43 ASN	8.278	113.23	54.5	37.61	175.8
44 GLN	7.475	115.79	63.75	37.62	175.88
45 ILE	6.763	122.86	60.82	39.55	
46 PRO			62.69	32.03	177.02
47 LYS	8.339	121.39	58.37	32.32	173.7
48 GLU	8.667	116.42	57.09	28.56	174.34
49 ALA	7.852	122.1	53.97	19.35	175.43
50 ASP	8.654	118.46	55.46	43.88	172.65
51 VAL	7.651	120.21	60.2	36.85	178.47
52 VAL	8.991	127.37	59	35.36	178.21
53 PHE	8.755	126.24	55.81	41.8	176.43
54 THR	8.493	114.76	60.41	70.39	179.28
55 GLN	8.028	121.23	55.6	29.88	179.01
56 GLU	8.724	120.93	60.5	29.91	179.02
57 ASN				36.79	175.55
58 LEU	7.553	119.51	54.19	43.28	177.94
59 ALA	7.133	123.11	56.21	18.88	179.03
60 GLU	8.517	118.09	59.59	28.97	177.95
61 ARG	7.922	119.93	58.64	30.05	176.99
62 ALA	8.407	120.81	55.38	17.83	173.9
63 ALA	7.671	117.32	53.95	18.44	175.95

Residue	HN	N	CA	CB	CO
64 GLN	7.257	114.02	57.51	28.6	177.12
65 VAL	7.398	119.83	65.53	32.56	174.46
66 VAL	7.64	110.84	57.34	32.68	175.76
67 PRO			64.75	32.14	177.08
68 HIS	8.053	112.87	55.65	30.7	174.81
69 ALA	7.172	123.78	51.79	19.34	178.53
70 LYS	7.834	121.89	55.71	33.21	177.94
71 ILE	8.63	127.78	58.73	36.39	178.31
72 VAL	9.231	132.57	61.43	32.21	174.32
73 THR	7.948	116.14	59.85	69.81	177
74 VAL	8.091	114.54	58.33	34.57	174.75
75 LYS	9.077	122.17	58.16	32.32	177.21
76 ASN	7.396	112.55	52.24	40.77	
77 PHE					
78 LEU					
79 ASP					
80 ASN					
81 THR					
82 VAL					
83 TYR	6.783	119.12	58.77	37.63	176.02
84 ILE	8.306	119.74	57.8	40.13	174.8
85 GLU	8.589	118.38	60.84	29.84	181.45
86 PHE	8.313	121.36	62.25	39.24	176.26
87 VAL	8.756	120.92	67.3	31.45	180.64
88 LYS	7.825	118.26	59.37	32.44	177.87
89 SER	7.632	114.57	60.55	63.31	179.67
90 LEU	7.033	121.48	55.29	41.86	179.23
91 ARG	7.622	119.06	55.77	31.45	174.02
92 LYS	7.893	127.72	58.02	33.71	

3.2. Protein interactions between *Tt*IIA^{Mtl} and *Tt*IIB^{Mtl}

3.2.1. Binding interfaces of the IIA^{Mtl}–IIB^{Mtl} complex of *T. tengcongensis*

NMR titrations were carried out to map the binding surfaces of the *Tt*IIA^{Mtl}–*Tt*IIB^{Mtl} complex. Chemical shift changes of backbone amide groups of ^{15}N-*Tt*IIA^{Mtl} were monitored, while titrating with *Tt*IIB^{Mtl} or phospho-*Tt*IIB^{Mtl}(C395S). Most of the chemical shift perturbation profiles is under 0.3ppm, indicating that the overall backbone has minimally changed upon complex formation.

In titration of *Tt*IIB^{Mtl}, the chemical shift changes were in the fast exchange regime on the chemical shift time scale (Figs. 13 and 14). Residues with large chemical shift perturbation were observed in the $\alpha2$–$\beta2$–$\beta3$, and slightly stronger shift in $\alpha3$ and $\alpha4$ regions. This result is consistent with the interaction surface of the *Ec*IIA^{Mtl} (Fig. 15 (A)). In the case of phospho-*Tt*IIB^{Mtl}(C395S) titration, the chemical shift changes were mostly in the fast exchange regime on the chemical shift time scale, except for several residues (Arg-49, Leu-52, Thr-55, Tyr-69, Glu-110, Ala-112, Lys-114, and Ile-137) that exhibited line broadening due to an intermediate exchange (Figs. 13 and 14). Residues with large chemical shift perturbation were observed in the $\alpha2$–$\beta2$–$\beta3$, $\beta5$, $\alpha3$, and $\alpha5$ regions, which was consistent with the interaction surface of the *Ec*IIA^{Mtl} (Fig. 15 (B)). The backbone amide chemical shifts of ^{15}N-phospho-*Tt*IIB^{Mtl}(C395S) titrating with *Tt*IIA^{Mtl} showed large chemical shift perturbations were observed in the $\beta1$– $\alpha1$ loop (active site P-loop), $\beta2$, and $\alpha2$ regions, which corresponded to the binding interface of phospho-*Ec*IIB^{Mtl}(C384S) (Fig. 15 (C)). Interfacial residues of IIA^{Mtl} were located at $\alpha2$ helix, $\alpha3$ helix, $\beta2$ strand, and $\beta3$ strand as well as the active site. Interfacial residues of IIB^{Mtl} were located at $\beta1$ strand, $\beta2$ strand, $\alpha1$ helix, and the active site loop region. The backbone fold and binding interfaces of the *Tt*IIA^{Mtl}–*Tt*IIB^{Mtl} complex closely

resembled those of the *Ec*IIA^{Mtl}–*Ec*IIB^{Mtl} complex (Fig. 16).

We also attempted to measure RDCs of the *Tt*IIA^{Mtl}–*Tt*IIB^{Mtl} complex, but could not find a proper alignment medium that was compatible with both of the proteins at the same time. *Tt*IIB^{Mtl} was compatible with phage *pf1* only under a high salt concentration that was deleterious to the complex formation with *Tt*IIA^{Mtl}. Other alignment media such as PEG/*n*-hexanol or polyacrylamide gel were not compatible with *Tt*IIA^{Mtl} or *Tt*IIB^{Mtl}.

Figure 13. Superimposed $^{1}H–^{15}N$ HSQC spectra of ^{15}N-IIA^{Mtl} of *T. tengcongensis* titrated with unphosphorylated *Tt*IIB^{Mtl} (left panel) and phosphorylated *Tt*IIB^{Mtl}(C395S) (right panel).

^{15}N-IIA^{Mtl} of *T. tengcongensis* titrated with unphosphorylated *Tt*IIB^{Mtl} (Left) The molar ratios are color-coded as follows: 0 (*black*), 1 (*red*), 2 (*orange*), 3 (*green*), 6 (*cyan*), 12 (*blue*), and 24 (*purple*) for IIB^{Mtl}. Selected residues with chemical shift perturbations are annotated in the spectra. ^{15}N-IIA^{Mtl} of *T. tengcongensis* titrated with phosphorylated *Tt*IIB^{Mtl} (C395S) (Right). The molar ratios are color-coded as follows: 0 (*black*), 0.5 (*red*), 1.0 (*orange*), 1.5 (*green*), 2.0 (*cyan*), 3.0 (*blue*) 4.0 (*purple*) for phospho-IIB^{Mtl}. Selected residues with chemical shift perturbation are annotated in the spectra.

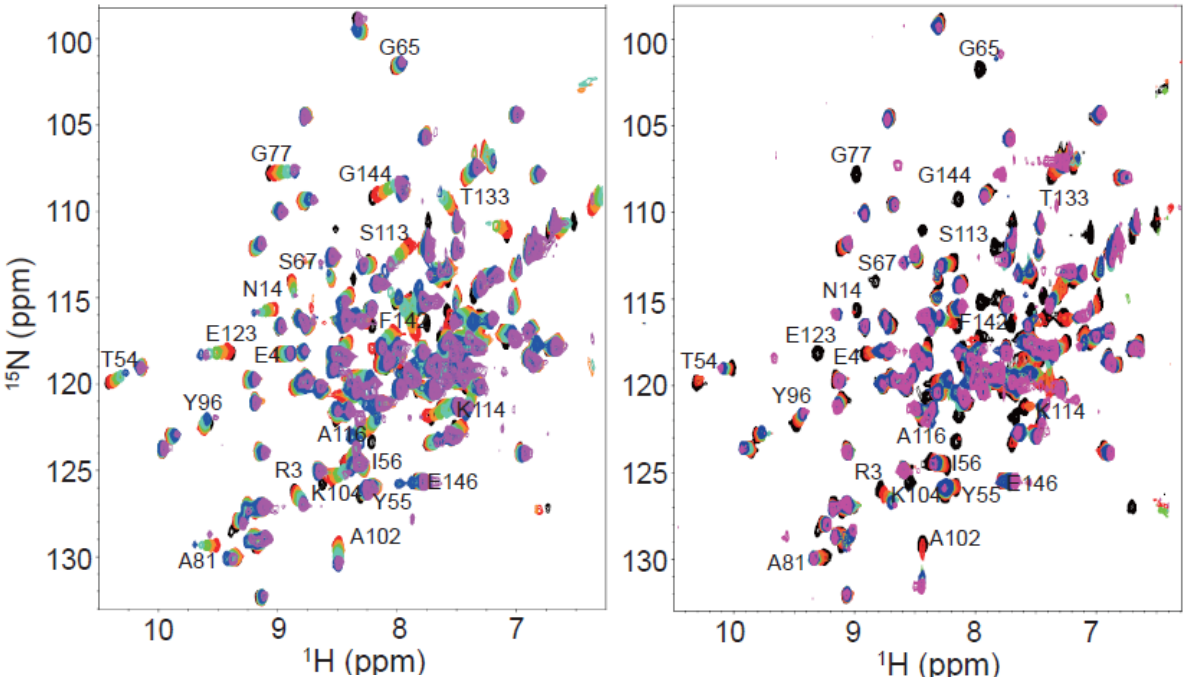
100
105
110
115
120
125
130
^{15}N (ppm)
10
9
8
7
^{1}H (ppm)
G65
G77
G144
T133
S113
S67
N14
E123
E4
T54
Y96
K114
A116
I56
R3
K104
Y55
E146
A102
A81

Figure 14. Close–up view of residues exhibiting different timescale of chemical shift.

Unphospho-*Tt*IIB^{Mtl} exhibited predominantly a fast exchange on the chemical shift time scale, however phospho-*Tt*IIB^{Mtl}(C395S) experiences in severe line-broadening due to an intermediate exchange.

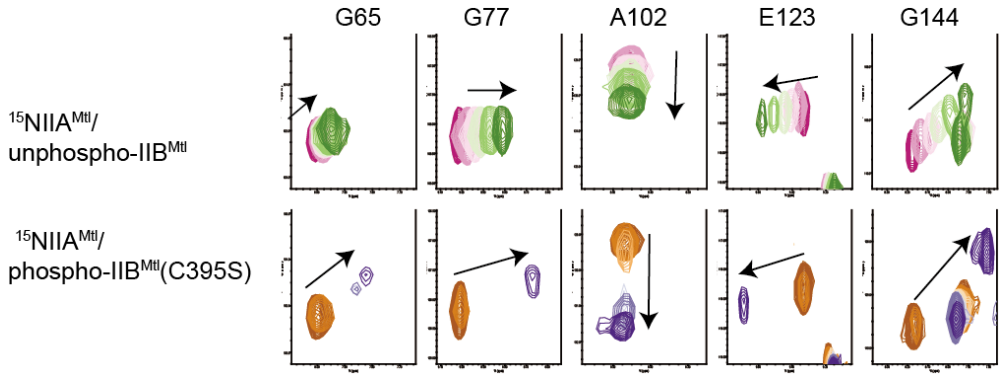
G65
G77
A102
E123
G144
^{15}NIIA^{Mtl}/
unphospho-IIB^{Mtl}
^{15}NIIA^{Mtl}/
phospho-IIB^{Mtl}(C395S)

Figure 15. Chemical shift perturbation of ^{15}N-*Tt*IIA^{Mtl} (A) titrated with *Tt*IIB^{Mtl}, ^{15}N-*Tt*IIA^{Mtl} titrated with phospho-*Tt*IIB^{Mtl}(C395S) (B) and ^{15}N-phospho-*Tt*IIB^{Mtl}(C395S) titrated with *Tt*IIA^{Mtl} (C).

Weighted $^{1}H_N/^{15}N$ chemical shift perturbation ($\Delta\delta = ([(\Delta\delta_{HN})^2 + (\Delta\delta_N)^2/25]/2)^{1/2}$ is plotted as a function of resudue number. Secondary structures are shown above the sequence.

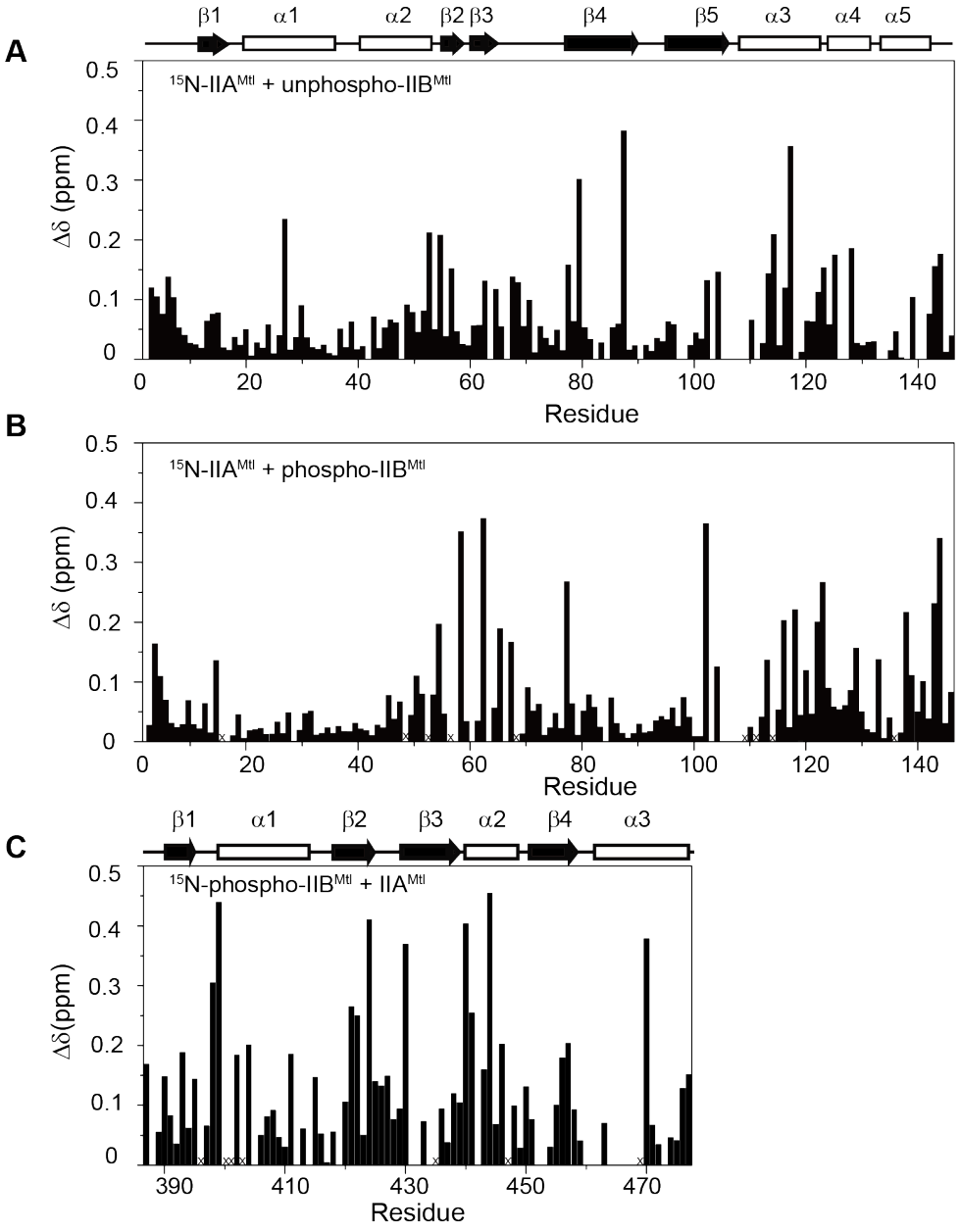
A
β1 α1 α2 β2 β3 β4 β5 α3 α4 α5
15N-IIAMtl + unphospho-IIBMtl
Δδ (ppm)
Residue
B
15N-IIAMtl + phospho-IIBMtl
Δδ (ppm)
Residue
C
β1 α1 β2 β3 α2 β4 α3
15N-phospho-IIBMtl + IIAMtl
Δδ(ppm)
Residue

Figure 16. Interface of *Tt*IIA^{Mtl}–*Tt*IIB^{Mtl} complex

The binding interfaces of the *Tt*IIA^{Mtl}–*Tt*IIB^{Mtl} complex has mapped on the complex structure of *Ec*IIA^{Mtl}–*Ec*IIB^{Mtl} (PDB code:2FEW). *Tt*IIA^{Mtl} is represented as a surface model colored in cyan and interface of *Tt*IIA^{Mtl}–*Tt*IIB^{Mtl} complex is colored in orange (upper panel). *Tt*IIB^{Mtl} is represented as a surface model colored in green and interface of *Tt*IIA^{Mtl}–*Tt*IIB^{Mtl} complex is colored in light orange (lower panel). The partner proteins are shown as ribbon diagram (left)

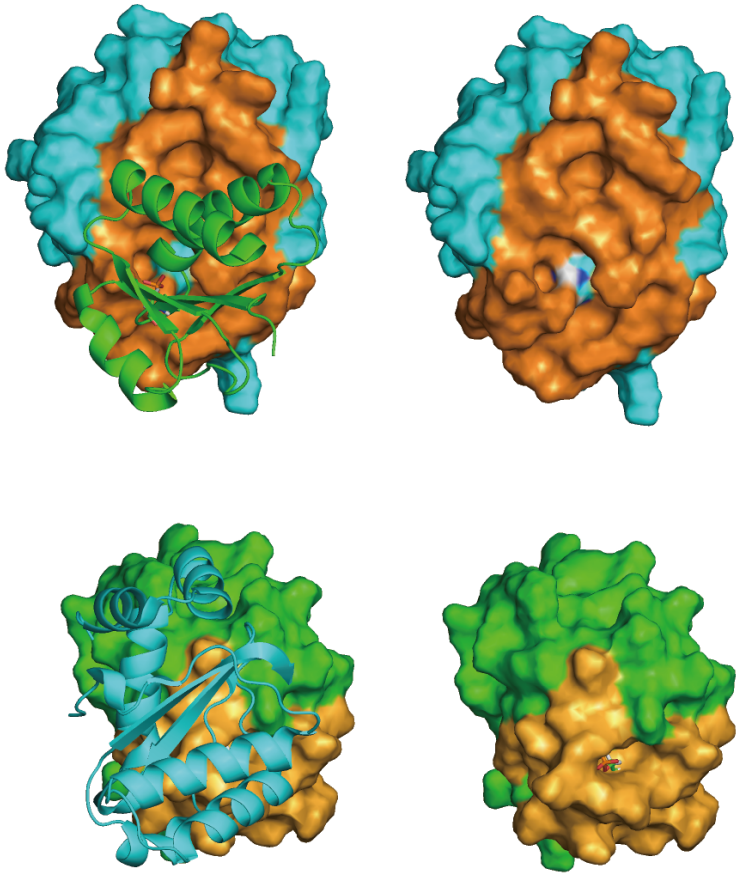

3.2.2. Equilibrium domain–domain association between *Tt*IIA^{Mtl} and *Tt*IIB^{Mtl}

Nonlinear least squares optimization of the titration data yielded the K_D values of 1.7±0.2 mM and 130±10 μM for *Tt*IIA^{Mtl}–*Tt*IIB^{Mtl} and *Tt*IIA^{Mtl}–phospho-*Tt*IIB^{Mtl}(C395S) complexes, respectively. (Figs. 17 and 18) The affinity increase upon phosphorylation was consistent with the observation that the titration with *Tt*IIB^{Mtl} exhibited predominantly a fast exchange on the chemical shift time scale, whereas the titration with phospho-*Tt*IIB^{Mtl}(C395S) resulted in severe line-broadening due to an intermediate exchange (Figs. 13 and 14). For example, Gly-65, Gly-77, Lys-104, Ser-113, Ala-116, Glu-123, and Gly-144 exhibited a fast exchange during the titration with IIB^{Mtl}, but showed line-broadening during the titration with phospho-*Tt*IIB^{Mtl} (C395S) (Fig. 13). Thus, phosphorylation increased the binding affinity between IIA^{Mtl} and IIB^{Mtl} of *T. tengcongensis* by twelve times, whereas it caused little changes in *E. coli.* System. This can be surprising given that the amino acid residues surrounding the phosphoryl group is well conserved between strains.

Within the global similarity, the different complex formations were originated form the details of the structure and the chemistry. To understand the driving forces that cause the large affinity increase, I compared the interfacial residues at the binding surface of the IIA^{Mtl}–IIB^{Mtl} complex between *T. tengcongensis* and *E. coli*. The binding interface has been well characterized between *Ec*IIA^{Mtl} and phospho-*Ec*IIB^{Mtl}(C384S)[34], and could be transferred to the *Tt*IIA^{Mtl}–phospho-*Tt*IIB^{Mtl}(C395S) complex binding interface based on the sequence alignment (Fig. 19).

The amino acid composition at the binding interface between IIA^{Mtl} and IIB^{Mtl} was investigated. The sequence similarity scores between *T. tengcongensis* and *E. coli* were 60% and 70% for IIA^{Mtl} and IIB^{Mtl}, respectively. The similarity scores of

interfacial residues, however, were 59% and 94% for IIA^{Mtl} and IIB^{Mtl}, respectively, indicating that the binding interface of IIB^{Mtl} is extremely well conserved (Figure. 16). Between *T. tengcongensis* and *E. coli*, 16 out of 27 interfacial residues were conserved in $IIA^{Mtl,}$ whereas 17 out of 18 interfacial residues were conserved in IIB^{Mtl}. Taken together, the data strongly suggests that the affinity change is largely attributed to the interface of IIA^{Mtl}. This assumption was supported by the measurement of cross-strain binding affinity, where the K_D value between *Tt*IIA^{Mtl} and phospho-*Ec*IIB^{Mtl}(C384S) was obtained as 120±30 μM, which was comparable to the binding affinity between *Tt*IIA^{Mtl} and phospho-*Tt*IIB^{Mtl}(C395S) (Table 6). On the other hand, the cross-strain binding between *Ec*IIA^{Mtl} and phospho-*Tt*IIB^{Mtl}(C395S) was very weak and produced little chemical shift changes during the titration.

Interfacial residues of *Tt*IIA^{Mtl} were identified to have responsibility for the affinity increase. Take notice of *Tt*IIA^{Mtl} associated with phospho-*Tt*IIB^{Mtl}(C395S) much stronger than with unphospho–*Tt*IIB^{Mtl}, indicating that phosphorylation provided a key binding surface. It has been reported that phosphorylation entails a small shift in the active site backbone loop of *Ec*IIB^{Mtl}, which stabilizes the phosphoryl group by a dense hydrogen bonding network.[33] I focused on the interfacial residues of *Tt*IIA^{Mtl} that provided intermolecular contacts with the phosphoryl group and also the surrounding loop region. Arg-538 and the active site His554 of *Ec*IIA^{Mtl} interacted with the phosphoryl group of phospho-*Ec*IIB^{Mtl}(C384S). Arg-538 made a salt bridge with the phosphoryl group, and His-554 was directly involved in the phosphoryl transfer reaction. Arg-538 and His-554 were highly conserved across most bacterial strains (Fig. 19). Residues that interacted with the active site loop surrounding the phosphoryl group were Thr-542, Thr-544, Gly-555, Thr-556, and Val-557. Among them, Thr-544 and Gly-555 were highly conserved across bacterial

strains, whereas Thr-542, Thr-556, and Val-557 were replaced by Ile-52, Val-66, and Ser-67 in *Tt*IIA^{Mtl} (Figs. 19 and 20). Thr-542 interacted with Asp-385 of *Ec*IIB^{Mtl}, while Thr-556 and Val-557 interacted with Ala-386 and Met-388 of *Ec*IIB^{Mtl}.

Figure 17. Equilibrium dissociation constants (K_D) derived from the CSP of ^{15}N-IIA^{Mtl} by (A) unphosphprylated IIB^{Mtl} and (B) phospho−IIB^{Mtl}(C395S).

All of the curves represent ^{1}H and ^{15}N shift perturbations. The lines represent nonlinear least squares best fits to all of the titration data simultaneously using a simple equilibrium binding model.

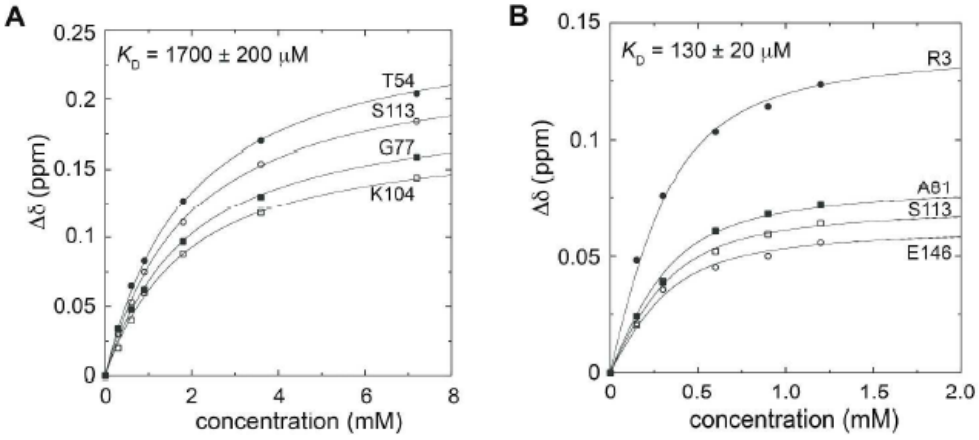
A
K_D = 1700 ± 200 μM
T54
S113
G77
K104
Δδ (ppm)
concentration (mM)
B
K_D = 130 ± 20 μM
R3
A81
S113
E146
Δδ (ppm)
concentration (mM)

Figure 18. Equilibrium dissociation constants (K_D) of ^{15}N-IIA^{Mtl} and phospho-IIB^{Mtl}(C395S) obtained by isothermal titration calorimetry.

Raw ITC data (top panels) and integrated heats of injection (bottom panels) from the titration between *Tt*IIA^{Mtl} and phospho-*Tt*IIB^{Mtl}(C395S). The squares are the experimental data and the lines represent the least-squares best-fit curve derived for one-set of sites binding model. The thermodynamic parameters are given in Table 6

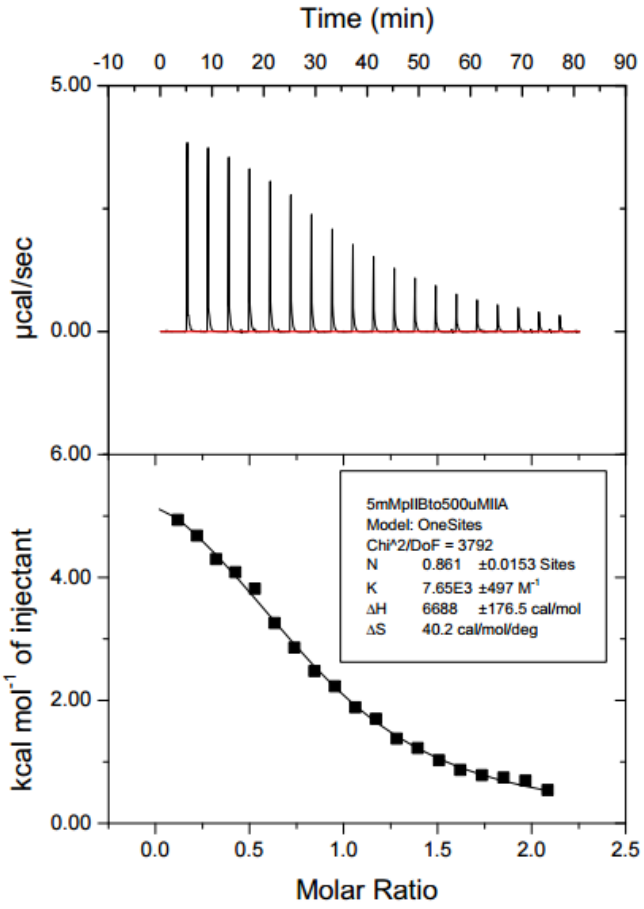
Time (min)
-10 0 10 20 30 40 50 60 70 80 90
5.00
0.00
µcal/sec
6.00
4.00
2.00
0.00
kcal mol-1 of injectant
0.0 0.5 1.0 1.5 2.0 2.5
Molar Ratio
5mMpIIBto500uMIIA
Model: OneSites
Chi^2/DoF = 3792
N 0.861 ±0.0153 Sites
K 7.65E3 ±497 M-1
ΔH 6688 ±176.5 cal/mol
ΔS 40.2 cal/mol/deg

Figure 19. Multiple sequence alignment of IIA^{Mtl} and IIB^{Mtl} between *Thermoanaerobacter tengcongensis*, *Escherichia coli*, *Yersinia pestis*, *Vibrio natriegens*, and *Bacillus. subtilis*.

Interfacial residues are marked with the asterisks, and the sequence similarity between the strains are color-coded in cyan (un-conserved), orange (similar) and red (conserved).

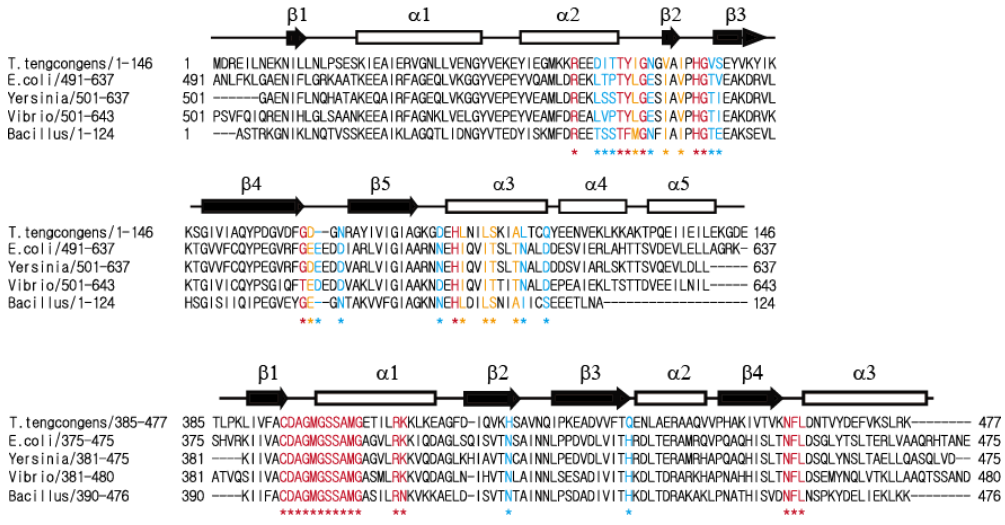
β1 α1 α2 β2 β3
T.tengcongens/1-146 1 MDRELLNEKNILLNLPSESKIEAIERVGNLLVENGYVVEKEYIEGMKKREEDITTYIGNGVAIPHGVSEYVKYIK
E.coli/491-637 491 ANLFKLGAENIFLGRKAATKEEAIRFAGEQLVKGGYVEPEYVQAMLDREKLTPTYLGESIAVPHGTVEAKDRVL
Yersinia/501-637 501 -------GAENIFLNQHATAKEQAIRFAGEQLVKGGYVEPEYVEAMLDREKLSSTYLGESIAVPHGTIEAKDRVL
Vibrio/501-643 501 PSVFQIQRENIHLGLSAANKEEAIRFAGNKLVELGYVEPEYVEAMFDREALVPTYLGESIAVPHGTIEAKDRVK
Bacillus/1-124 1 ---ASTRKGNIKLNQTVSSKEEAIKLAGQTLIDNGYVTEDYISKMFDREETSSTFWGNFIAIPHGTEEAKSEVL
β4 β5 α3 α4 α5
T.tengcongens/1-146 KSGIVIAQYPDGVDFGD--GNRAYIVIGIAGKGDEHLNILSKIALTCQYEENVEKLKKAKTPQEIIEILEKGDE 146
E.coli/491-637 KTGVVFCQYPEGVRFGEEDDIARLVIGIAARNNEHIQVITSLTNALDDESVIERLAHTTSVDEVLELLAGRK- 637
Yersinia/501-637 KTGVVFCQYPEGVRFGDEEDDVARLVIGIAARNNEHIQVITSLTNALDDDSVIARLSKTTSVQEVLDLL----- 637
Vibrio/501-643 KTGIVICQYPSGIQFTEDEDDVAKLVIGIAAKNDEHIQVITTITNALDEPEAIEKLTSTTDVEEILNIL----- 643
Bacillus/1-124 HSGISIIQIPEGVEYGE--GNTAKVVFGIAGKNNEHLDILSNIAIICSEEETLNA---------- 124
β1 α1 β2 β3 α2 β4 α3
T.tengcongens/385-477 385 TLPKLIVFACDAGMGSSAMGETILRKKLKEAGFD-IQVKHSAVNQIPKEADVVFTQENLAERAAQVVPHAKIVTVKNFLDNTVYDEFVKSLRK-------- 477
E.coli/375-475 375 SHVRKIIVACDAGMGSSAMGAGVLRKKIQDAGLSQISVTNSAINNLPPDVDLVITHRDLTERAMRQVPQAQHISLTNFLDSGLYTSLTERLVAAQRHTANE 475
Yersinia/381-475 381 -----KIIVACDAGMGSSAMGAGVLRKKVQDAGLKHIAVTNCAINNLPEDVDLVITHRDLTERAMRHAPQAQHISLTNFLDSQLYNSLTAELLQASQLVD-- 475
Vibrio/381-480 381 ATVQSIIVACDAGMGSSAMGASMLRKKVQDAGLN-IHVTNLAINNLSESADIVITHKDLTDRARKHAPNAHHISLTNFLDSEMYNQLVTKLLAAQTSSAND 480
Bacillus/390-476 390 -----KIIFACDAGMGSSAMGASILRNKVKKAELD-ISVTNTAINNLPSDADIVITHKDLTDRAKAKLPNATHISVDNFLNSPKYDELIEKLKK-------- 476

Figure 20. Conservation mapping of the interface based on the similarity between *T.tengcongensis* and *E.coli.*

Interfacial residues are color-coded on the surface of brown colored IIA^{Mtl} and purple colored IIB^{Mtl} in cyan (un-conserved), orange (similar) and red (conserved).

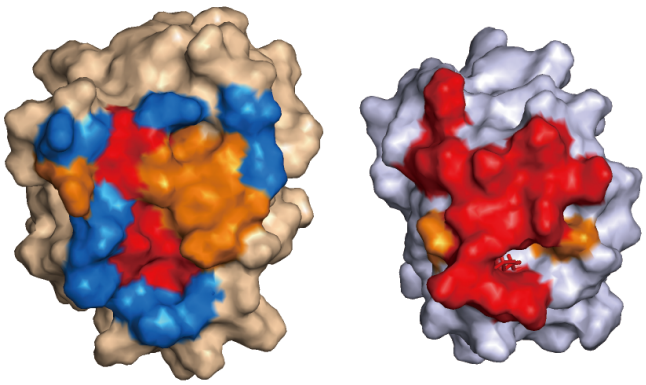

IIA^{Mtl} IIB^{Mtl}

Table 6. Equilibrium dissociation constants (K_D) between IIA^{Mtl} and phospho-IIB^{Mtl} of *E.coli* and *T. Tengcongensis* in various combinations obtained by NMR titration[a] and ITC[b]

IIA^{Mtl}	IIB^{Mtl}	K_D (μM)	ΔH (kcal/mol)	ΔS (cal/mol/deg)
EcIIA^{Mtl}	phospho-*Ec*IIB^{Mtl}(C384S)	3700 ± 200 [a]		
TtIIA^{Mtl}	unphospho-*Tt*IIB^{Mtl}	1700 ± 200 [a]		
EcIIA^{Mtl}	unphospho-*Tt*IIB^{Mtl}	N.D. [a, b]		
TtIIA^{Mtl}	phospho-*Tt*IIB^{Mtl}(C395S)	130 ± 10 [c]	6.7 ± 0.2	40.2
TtIIA^{Mtl}	phospho-*Ec*IIB^{Mtl}(C384S)	120 ± 30 [c]	1.4 ± 0.1	22.5

[a] Determined by nonlinear least squares best fits to NMR titration data in 20 mM Tris, pH 7.4, at 25ºC (see Materials and methods for detail).

[b] Not determined due to the lack of chemical shift changes

[c] Determined by ITC data analysis using one-set of sites binding mode. ITC experiments were performedl in 20 mM Tris, pH 7.4, at 25ºC.

3.2.3. Temperature dependent interaction

In previous sections, all studies have done at room temperature which is sufficient for having insight upon activity of mesophilic *E. coli*. However, functional study of thermophilic *T. tengcongensis* has not revealed at the physiological temperature, 75ºC. To understand interaction of the *T. tengcongensis* at natural growth temperature, thermodynamic parameters were examined using ITC experiments over a range of temperatures (25, 35, 45, 55, 65, and 75 ºC).

The K_D of *T. tengcongensis* showed minimal effect on the temperature variation (Table. 7). At 45 ºC and 55ºC, the enthalpic contribution to the Gibbs free energy shows around zero, this can easily overestimate or underestimate the entropic contribution. Thus, the thermodynamic fitting curve might have large error and leads ambiguous entropic term Even if the solid energetic correlation is hidden from the view, results demonstrate the interactions are entropy driven, The hydrophobic interaction maintains the complex forming mechanism by displacing the water molecule form the interface to adapt in higher temperature.

Table 7. Temperature dependence of equilibrium dissociation constants (K_D) between IIA^{Mtl} and phospho-IIB^{Mtl}(C395S) of *T. tengcongensis.*

Temperature ºC(K)	K_D (μM)	ΔH (kcal/mol)	ΔS (cal/mol/deg)	ΔG (kcal/mol)
25 ºC (298K)	130 ± 10	6.7 ± 0.2	40.2	-5.3 ± 0.4
35 ºC (308K)	110 ± 17	1.4 ± 0.07	22.7	-5.6 ±0.8
45 ºC (318K)	95 ± 45[a]	0.4 ± 0.04	19.7[a]	-5.8 ± 2.8[a]
55 ºC (328K)	120 ± 80[a]	0.5 ± 0.05	18.3[a]	-5.5 ± 2[a]
65 ºC (338K)	92 ± 21	-0.6 ± 0.05	16.6	-6.2 ± 1.4
75 ºC (348K)	53 ± 8	-1.5 ± 0.07	15.2	-6.8 ± 1.0

[a] Large error due to small enthalpy value, binding fitting curve fluctuates even with small deviation of parameter.

3.3 Mutational study

Based on the differences in the interfacial residues, thermophilic-like *Ec*IIA^{Mtl} mutants has been designed to have a higher affinity with respect to the phospho-*Ec*IIB^{Mtl}(C384S). Nevertheless, phosphorylation enhanced the interaction between the domains A and B through the direct covalent bonds with the phosphoryl group that are highly conserved between strains (Fig. 19). I have pay attention into the indirect interaction with the phosphoryl group that is interacting with the overall stabilized active site loop. The residues at *Ec*IIA^{Mtl} interface within 6Å of the active site loop are considered to have responsibility to the indirect interaction by phosphorylation. Among them the residues are unconserved through the strains has designed to the mutants. The *Ec*IIA$^{Mtl}_{M1}$ mutant contained two mutations at the end of the α2 helix (T542I/P543T), and the *Ec*IIA$^{Mtl}_{M2}$ mutant contained two mutations (T556V/V557S) next to the active site His-554, and the *Ec*IIA$^{Mtl}_{M3}$ mutant at the loop between the β5 and α3 (N598D) (Table. 8 and Fig. 21). The equilibrium binding constants between *Ec*IIA^{Mtl} mutants and phospho-*Ec*IIB^{Mtl}(C384S) were measured by ITC, and both mutants *Ec*IIA$^{Mtl}_{M1}$ and *Ec*IIA$^{Mtl}_{M2}$, exhibited a significant increase in the binding affinity, while *Ec*IIA$^{Mtl}_{M3}$ showed such a weak affinity that the binding heat could not be detected.

*Ec*IIA$^{Mtl}_{M1}$ showed 45 times stronger binding (K_D = 82±23 μM), and *Ec*IIA$^{Mtl}_{M2}$ showed 19 times stronger binding (K_D = 200±60 μM) compared wild-type *Ec*IIA^{Mtl} (Table. 9). To explain the structural basis for the increased affinity, I examined the interface of each *Ec*IIA^{Mtl} mutant in complex with phospho-*Ec*IIB^{Mtl}(C384S). *Ec*IIA$^{Mtl}_{M1}$ achieved a high affinity mainly via hydrophobic cluster formation proximal to the active site loop. Ile-542 of *Ec*IIA$^{Mtl}_{M1}$ provided favorable hydrophobic interactions with Leu-433 and Phe-452 of phospho-*Ec*IIB^{Mtl}(C384S), which could reinforce the interaction of the α2 helix of *Ec*IIA$^{Mtl}_{M1}$ with the active

site loop of phospho-*Ec*IIB^{Mtl}(C384S) (Figure. 22). In *Ec*IIA$^{Mtl}_{M2}$, the hydroxyl group of Ser-557 of *Ec*IIA$^{Mtl}_{M2}$ provided a hydrogen bond to the backbone carbonyl group of Ala-386 of *Ec*IIB^{Mtl}, which could strengthen the interaction of Arg538 and His-554 of *Ec*IIA$^{Mtl}_{M2}$ with the phosphoryl group of phospho-*Ec*IIB^{Mtl}(C384S)

Table 8. *Ec*IIA^{Mtl} mutation site and position in the structure.

Mutants	Mutation residue	Position of the mutation site in the structure
*Ec*IIA$^{Mtl}_{M1}$	T542I, P543T	C–terminal of α2 helix
*Ec*IIA$^{Mtl}_{M2}$	T556V,V557S	Loop between the β3 and β4
*Ec*IIA$^{Mtl}_{M3}$	N598D	Loop between the β5 and α3

Figure 21. Mutation sites of the *Ec*IIA^{Mtl}.

Three-dimensional structure of the enzyme *Ec*IIA^{Mtl} from *E.coli* (PDB entry 2FEW chain A) is shown in ribbon diagram. The mutation sites are introduced by space-filling model. The *Ec*IIA$^{Mtl}_{M1}$ mutant contained two mutations at the end of the α2 helix (T542I/P543T), and the *Ec*IIA$^{Mtl}_{M2}$ mutant contained two mutations (T556V/V557S) next to the active site His554. The *Ec*IIA$^{Mtl}_{M3}$ has N598D mutation at the loop between the β5 and α3 (N598D). The active site residue His-554 has shown in stick.

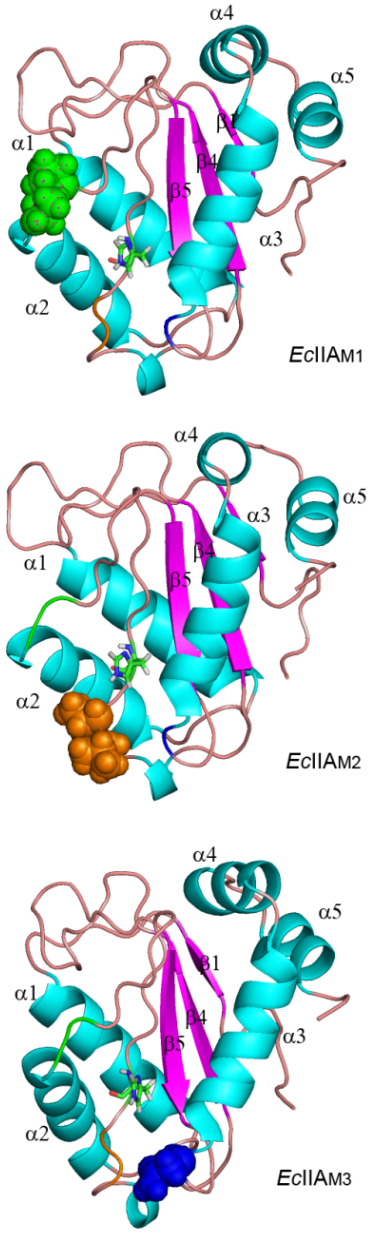
α4
α5
β1
α1
β4
β5
α3
α2
EcIIAM1
α4
α3
α5
β4
α1
β5
α2
EcIIAM2
α4
α5
β1
α1
β4
β5
α3
α2
EcIIAM3

Table 9. Equilibrium dissociation constants (K_D) between IIA^{Mtl} and phospho-IIB^{Mtl} of *E. coli* and *T. tengcongensis* in various combinations obtained by NMR titration[a] and ITC[b].

IIA^{Mtl}	IIB^{Mtl}	K_D (μM)	ΔH (kcal/mol)	ΔS (cal/mol/deg)
EcIIA^{Mtl}	phospho-*Ec*IIB^{Mtl}(C384S)	3700 ± 200 [a]		
TtIIA^{Mtl}	phospho-*Tt*IIB^{Mtl}(C395S)	130 ± 10 [b]	6.7 ± 0.2	40.2
TtIIA^{Mtl}	phospho-*Ec*IIB^{Mtl}(C384S)	120 ± 30 [b]	1.4 ± 0.1	22.5
EcIIA_{M1}	phospho-*Ec*IIB^{Mtl}(C384S)	82 ± 20 [b]	0.4 ± 0.1	19.9
EcIIA_{M2}	phospho-*Ec*IIB^{Mtl}(C384S)	200 ± 60 [b]	0.7 ± 0.1	19.4
EcIIA_{M3}	phospho-*Ec*IIB^{Mtl}(C384S)	N.D. [b, c]		

[a] Determined by nonlinear least squares best fits to NMR titration data in 20 mM Tris, pH 7.4, at 25ºC (see Materials and methods for detail).

[b] Determined by ITC using one-set of sites binding model in 20 mM Tris, pH 7.4, at 25ºC.

[c] Not determined due to the lack of heat changes

Figure 22. The detail interaction at the binding interfaces between *Ec*IIA^{Mtl} and phospho-*Ec*IIB^{Mtl}(C384S) (PDB code 2FEW).

Left panels represent the interfaces of the *Ec*IIA^{Mtl}–phospho-*Ec*IIB^{Mtl}(C384S) complex, and *right* panels represent the interfaces of (A) the *Ec*IIA$_{M1}$–phospho-*Ec*IIB^{Mtl}(C384S) complex, and (B) the *Ec*IIA$_{M2}$–phospho-*Ec*IIB^{Mtl}(C384S) complex. Interfacial residues are annotated am\nd mutations sites of the *Ec*IIA^{Mtl} mutants are labeld in *red*. Interfacial residues of phospho-*Ec*IIB^{Mtl}(C384S) are labeled in *italic type*. The hydrophobic cluster formed by I542 of *Ec*IIA$_{M1}$, and *L433* and *F452* of phospho-*Ec*IIB^{Mtl}(C384S) is highlighted by a *yellow* shade. The hydrogen bonding formed by S557 of *Ec*IIA$_{M2}$ and *A386* of phospho-*Ec*IIB^{Mtl}(C384S) is highlighted by a thick dashed line.

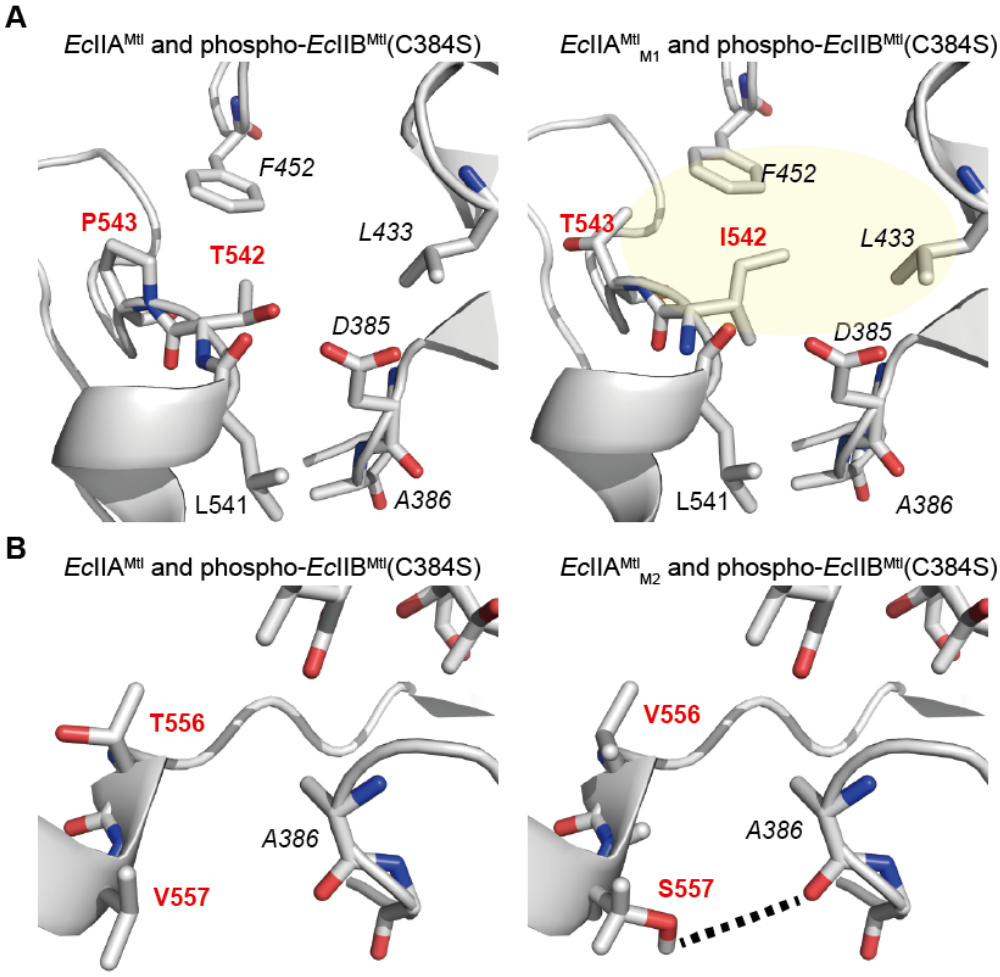
A
EcIIA^Mtl and phospho-EcIIB^Mtl(C384S)
F452
P543
T542
L433
D385
L541
A386
EcIIA^Mtl_M1 and phospho-EcIIB^Mtl(C384S)
F452
T543
I542
L433
D385
L541
A386
B
EcIIA^Mtl and phospho-EcIIB^Mtl(C384S)
T556
A386
V557
EcIIA^Mtl_M2 and phospho-EcIIB^Mtl(C384S)
V556
A386
S557

4. Discussion

The *Tt*IIA^{Mtl} and *Tt*IIB^{Mtl}(C395S) domains show similar backbone folds to the homologous *Ec*IIBA^{Mtl} domain, with 40% sequence identity and 60% sequence similarity between strains. Moreover, the interface of individual domains was found to be well conserved between *E. Coli* and *T. t*. In this study, only a few mutations at the domain interface were sufficient to maintain the domain associations of Enzyme II^{Mtl} in response to gain or loss of the linker. The mutants not only alter the local chemistry, but also affect the overall interfacial character. Analysis of the *Ec*IIA^{Mtl}–phospho-*Ec*IIA^{Mtl}(C384S) complex showed that two conserved hydrophobic methionine pockets are essential as molecular recognition anchors at the top halves and bottom halves.[34] The mutant *Ec*IIA$_{M1}$ showed additory hydrophobic interactions between the pockets that can bridge them together and expand the hydropohbic cluster across the board. For the mutant *Ec*IIA$_{M2}$, Val-556 was founded to contribute to the bottom pocket hydrophobic interactions instead of Ser-557 substituted for valine, and the hydrogen bond of Ser-557 wrap up the interface at the border (Fig. 23).

Furthermore, the interaction between *Tt*IIA^{Mtl} and *Tt*IIB^{Mtl} showed highly sensitivity to the phosphorylation state. From the structural aspects, the phosphorylation of *Tt*IIB^{Mtl} effectively suppressed the conformational dynamics at the active site loop, providing a ready-made recognition motif for *Tt*IIA^{Mtl}. To compare the molecular recognition mode with or without phosphorylation, ^{15}N-*Tt*IIA^{Mtl} and identical molar ratios of the titrants were determined as depicted in Figure 24. For the *Tt*IIA^{Mtl} and unphospho–*Tt*IIB^{Mtl}(C395S) complex, weak CSPs appeared at the overall interface, and slightly stronger CSPs were clustered upon top of the hydrophobic pocket (residues 110–130). However, there were no significant shifts detected in the functional site, and thus the specific interaction is not yet clear.

Even though the affinity is weak, it nevertheless suficiente to enhances interactions in the searching for binding partners and acts as a basal state. The *Tt*IIA^{Mtl}and phospho–*Tt*IIB^{Mtl}(C395S) complex showed a different tendency, with a dramatic shift clustered at both the top and bottom hydrophobic pockets, and specific CSPs are arose in proximity to the active site (residues 49–76 and 110–130). Presumably the methionine pocket recognizes the phospho–*Tt*IIB^{Mtl}(C395S) and the proximity residues *Ec*IIA$_{M1}$ and *Ec*IIA$_{M2}$, located at the specific region to forming a stable complex and thus enabling a functionally proper interaction. Taken together, these results suggest that non-fruitful unphosphorylated *Tt*IIB^{Mtl} experiences faster turnover that inhibits meaningless encounters between domains and dissociates further away to search for a fruitful partner. East acess to the fruitful partner phospho–*Tt*IIB^{Mtl} is mediated by strong and specific interactions easily access to the partner, suppressing futile associations between unphosphorylated proteins.

The cellular concentrations of *Tt*IIA^{Mtl} and *Tt*IIB^{Mtl} have not been experimentally determined, but can be roughly estimated at ~40μM and ~10μM, respectively, according to reported values of the glucose transporter Enzyme II^{Glc}.[39,52] The estimated concentrations and the measured K_D value predict that unphospho–*Tt*IIB^{Mtl} would form a complex with *Tt*IIA^{Mtl} ~ 0.5% of the times and phospho–*Tt*IIB^{Mtl} forms ~23% of the time. The functional state is remarkably similar to ~30% of the bound fractions observed for *Ec*IIA^{Mtl} and *Ec*IIB^{Mtl}, regardless of the linker. The enhanced affinity effectively compensates for the loss of the linker, enabling domain associations in the cell to be maintained at an optimal level. In this manner, domain interactions could be conserved across the bacterial kingdoms.

The protein activity is not only the explained by equilibrium state, but the kinetics between the proteins are also orchestrated in a precise and time-dependent manner, underlying their cellular function. The kinetic study of the A and B domains

of *Ec*IIBA^{Mtl} demonstrated that the interaction between the linker connected domain is derived rapid association and dissociation; however, the enzymatic activity was not coupled to the interactions, which was 40-fold slower than the molecular recognition.[36] Thus, to further elucidate and compare the mechanism of enzymatic activity for *Tt*IIA^{Mtl} and *Tt*IIB^{Mtl}, the specific kinetic parameters, i.e., association rate and dissociation rate might be considered. Determination of the origin of affinity from rapid association and/or from slower dissociation, it might help to gain better understanding of the actual phosphotransfer reaction. Furthermore, more detailed comprehension of the functional reaction will provide a clue into linker loss evolution pressure.

Figure 23. Overall interaction alternated by *Ec*IIA^{Mtl} mutants (PDB code 2FEW).

Upper panels represent the interfaces of the *Ec*IIA^{Mtl} mutant. Mutational residues of *Ec*IIA^{Mtl} are colored in *green*, and interacting residues of phospho-*Ec*IIB^{Mtl}(C384S) are colored in *red* stick model and *Ec*IIA$_{M2}{}^{Mtl}$ interacting residue is colored in *yellow* stick model. Top halves hydrophobic methionine pockets are colored in *light blue* and bottoms in *blue*. Hydrophobic cluster is expanded and wraped up by *Ec*IIA^{Mtl} mutants. *Lower* panel represents the complex of surface represneted *Ec*IIA^{Mtl} mutant and cartoon represented phospho-*Ec*IIB^{Mtl}(C384S).

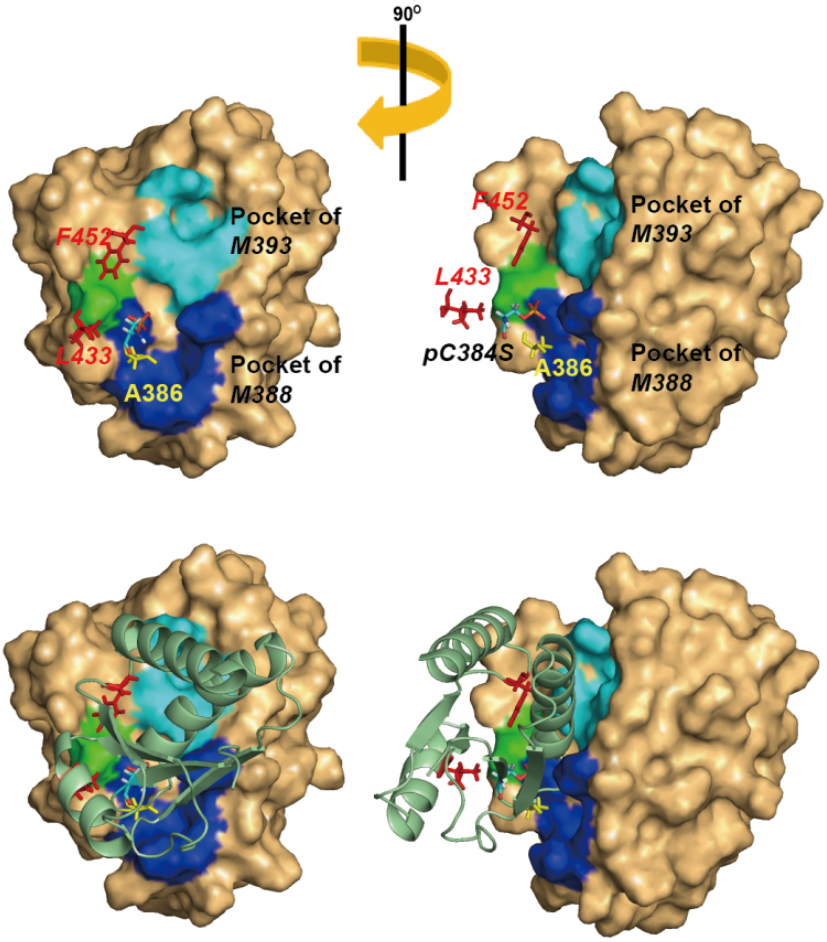
90°
F452
Pocket of
M393
L433
A386
Pocket of
M388
F452
Pocket of
M393
L433
pC384S
A386
Pocket of
M388

Figure 24. Basal state and functional state of the *Tt*IIA^{Mtl}-*Tt*IIB^{Mtl} complex.

Left panel represents CSP of 0.3mM ^{15}N-*Tt*IIA^{Mtl}-1.2mM phospho-*Tt*IIB^{Mtl} (*Black* bar) and 0.3mM ^{15}N-*Tt*IIA^{Mtl}-1.2mM unphospho-*Tt*IIB^{Mtl} (*Black* bar). The chemical shift difference shows dramatic upon phosphorylation has represented as shade box (*orange*). *Right* panel represents boxed regions upon the structure in surface model. *Ec*IIA$_{M1}$ and *Ec*IIA$_{M2}$ are labeled on the functional region.

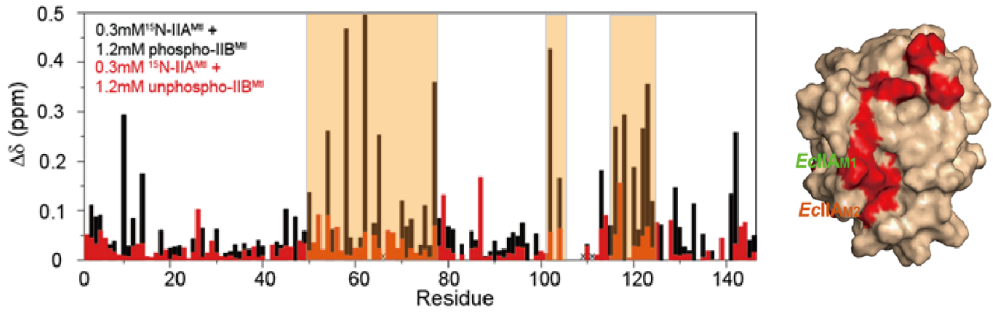
0.3mM 15N-IIAMtl +
1.2mM phospho-IIBMtl
0.3mM 15N-IIAMtl +
1.2mM unphospho-IIBMtl
Δδ (ppm)
0.5
0.4
0.3
0.2
0.1
0
0
20
40
60
80
100
120
140
Residue
EcIIAmt
EcIIAmt

5. References

1. Shi Y and Wu J., Structural basis of protein-protein interaction studied by NMR. *J Struct Funct Genomics.* 2007 Sep;8(2-3):67-72
2. Baronti L et al., Dynamics of the intrinsically disordered C-terminal domain of the nipah virus nucleoprotein and interaction with the x domain of the phosphoprotein as unveiled by NMR spectroscopy. *Chembiochem.* 2015 Jan 19;16(2):268
3. Vogel C et al., Structure, function and evolution of multidomain proteins, *Curr Opin Struct Biol.* 2004 Apr;14(2):208–16.
4. Reddy Chichili VP et al., Linkers in the structural biology of protein-protein interactions. *Protein Sci.* 2013;22(2):153–67.
5. Krishnamurthy VM et al., Dependence of effective molarity on linker length for an intramolecular protein-ligand system. *J Am Chem Soc.* 2007;129(5):1312–20.
6. Bhandari D.G et al., ^{1}H-NMR study of mobility and conformational constraints within the proline-rich N-terminal of the LC1 alkali light chain of skeletal myosin. Correlation with similar segments in other protein systems. *Eur. J. Biochem.* 1986;160:349–356.
7. Burton J et al., Conformational preferences of sequential fragments of the hinge region of human IgA1 immunoglobulin molecule: II. *Biophys. Chem.* 1989;33: 39–45.
8. Ferreira L.M et al., Spatial separation of protein domains is not necessary for catalytic activity or substrate binding in a xylanase. *Biochem. J.* 1990; 269: 261–264.
9. Radford S.E et al., Conformational flexibility and folding of synthetic peptides representing an interdomain segment of polypeptide chain in the pyruvate dehydrogenase multienzyme complex of Escherichia coli. *J. Biol. Chem.* 1989; 264: 767–775
10. Pratt D et al., Fundamentals of biochemistry : life at the molecular level (2. ed.). Hoboken, NJ: Wiley. (2006).ISBN 0-471-21495-7.
11. Barford D et al., The structure and mechanism of protein phosphatases: insights into catalysis and regulation. *Annu Rev Biophys Biomol Struct* 1998; 27: 133–64.
12. Cohen P., The regulation of protein function by multisite phosphorylation: a 25-year update. *Trends in Biochemical Science* 2000;25: 596–601
13. Cieśla J et al., Phosphorylation of basic amino acid residues in proteins: important but easily missed. *Acta Biochim Pol.* 2011;58(2):137-48.
14. Cole PA et al., Protein tyrosine kinases Src and Csk: a tail's tale. *Curr Opin Chem Biol* 2003; 7 (5): 580–5.
15. Babior BM., NADPH oxidase: an update. *Blood* 1999; 93 (5): 1464–76.
16. Li-Rong Y et al., Phosphoproteomics for the discovery of kinases as cancer biomarkers and drug targets, *Proteomics: Clinical Applications*, 2007; 1 (9): 1042–1057.
17. Tanji K et al., Phosphorylation of serine 349 of p62 in Alzheimer's disease brain. *Acta Neuropathol Commun*. 2014;2:50.
18. Zhang Y et al., Phosphorylation of Histone H2A Inhibits Transcription on Chromatin Templates. *J. Biol. Chem* 2004; 279 (21): 21866–21872
19. Qian X et al., Inhibition of p38 MAPK Phosphorylation Is Critical for Bestatin to Enhance ATRA-Induced Cell Differentiation in Acute Promyelocytic Leukemia NB4 Cells. *Am J Ther*. 2016;23(3):e680-9.
20. Offringa R and Huang F., Phosphorylation-dependent trafficking of plasma membrane proteins in animal and plant cells. *J Integr Plant Biol*. 2013;55(9):789-808.

21. Walker DG and Rao S., The role of glucokinase in the phosphorylation of glucose by rat liver. *Biochemical Journal* 1964; 90 (2): 361.
22. Villar-Palasí, C and Guinovart, J. J., The role of glucose 6-phosphate in the control of glycogen synthase. *The FASEB Journal* 1997;11 (7): 544–558.
23. Nguyen LK, et al., When ubiquitination meets phosphorylation: a systems biology perspective of EGFR/MAPK signalling. *Cell Commun Signal.* 2013;11:52.
24. Sólyom Z, et al., The Disordered Region of the HCV Protein NS5A: Conformational Dynamics, SH3 Binding, and Phosphorylation. *Biophysical* 2015; 109 (7): 1483-1496
25. Meadow ND et al.,The bacterial phosphoenolpyruvate: glycose phosphotransferase system. *Annu Rev Biochem* 1990;59:497–542.
26. Postma PW et al., Phosphoenolpyruvte: carbohydrate phosphotransferase system of bacteria. *Microbiol Rev* 1993;57:543–594
27. Deutscher J et al., How phosphotransferase system-related protein phosphorylation regulates carbohydrate metabolism in bacteria. *Microbiol Mol Biol Rev* 2006;70:939–1031.
28. Robillard GT and Lolkema JS., Enzymes-II of the Phosphoenolpyruvate-Dependent Sugar-Transport Systems - a Review of Their Structure and Mechanism of Sugar-Transport. *Biochimica Et Biophysica Acta.* 1988;947(3):493–519.
29. Lengeler JW et al., Enzymes II of the phosphoenolpyruvate-dependent phosphotransferase systems: their structure and function in carbohydrate transport. *Biochim Biophys Acta* 1994;1188:1–28
30. van Weeghel RP et al., Cytoplasmic phosphorylating-domain of the mannitol-specific transport protein of the phosphoenolpyruvate-dependent phosphotransferase system in *Escherichia coli*: overexpression, purification and functional complementation with the mannitol binding domain. *Biochemistry* 1991;30:9478–9485.
31. van Montfort RLM et al., The structure of the *Escherichia coli* phosphotransferase $IIA^{mannitol}$ reveals a novel fold with two conformations of the active site. *Structure* 1998; 6:377–388.
32. Legler PM et al., Three-dimensional solution structure of the cytoplasmic B domain of the mannitol transporter IImannitol of the *Escherichia coli* phosphotransferase system. *J Biol Chem* 2004;279:39115–39121.
33. Suh JY et al., Visualization of the phosphorylated active site loop of the cytoplasmic B domain of the mannitol transporter $II^{Mannitol}$ of the *Escherichia coli* phosphotransferase system by NMR spectroscopy and residual dipolar couplings. *J Mol Biol* 2005; 353:1129–1136.
34. Suh JY et al., Solution structure of a post-transition state analog of the phosphotransfer reaction between the A and B cytoplasmic domains of the mannitol transporter $II^{Mannitol}$ of the *Escherichia coli* phosphotransferase system. *J Biol Chem* 2006;281:8939–8949.
35. G Cornilescu et al., Cytoplasmic A Domain of the Mannitol Transporter IIMannitol and HPr of the Escherichia coliPhosphotransferase System *J Biol Chem* 2002; 277 (44), 42289-42298
36. Suh JY et al., Intramolecular domain-domain association/dissociation and phosphoryl transfer in the mannitol transporter of *Escherichia coli* are not coupled. *Proc Natl Acad Sci USA* 2007;104:3153–3158.
37. Bao Q et al., A complete sequence of the T. tengcongensis genome. *Genome Res* 2002;12:689–700.
38. Lee KO and Suh JY., ^{1}H, ^{15}N, and ^{13}C backbone assignments and secondary structure

of the cytoplasmic domain A of mannitol trasporter $II^{Mannitol}$ from *Thermoanaerobacter Tencongensis* phosphotransferase system. *J Kor Magn Reson Soc* 2015;19:42–48
39. Rohwer JM et al., Understanding glucose transport by the bacterial phosphoenolpyruvate:glycose phosphotransferase system on the basis of kinetic measurements in vitro. *J Biol Chem* 2000;275:34909–34921
40. Delaglio F et al., NMRPipe: a multidimensional spectral processing system based on UNIX pipes. *J Biomol NMR* 1995;6:277–293.
41. Garrett DS et al., A common sense approach to peak picking in two-, three-,and four-dimensional spectra using automatic computer analysis of contour diagrams. *J Magn Reson* 1991;95:214–220.
42. Johnson BA and Blevins RA., NMRView: A computer program for the visualization and analysis of NMR data. *J Biomol NMR* 1994;4:603–614.
43. Yang Shen and Ad Bax., SPARTA+: a modest improvement in empirical NMR chemical shift prediction by means of an artificial neural network *J. Biomol. NMR* 2010; 48: 13-22.
44. Williamson MP., Using chemical shift perturbation to characterise ligand binding. *Prog Nucl Magn Reson Spectrosc.* 2013;73:1-16
45. Bax A et al., Dipolar couplings in macromolecular structure determination. *Methods Enzymol* 2001;339:127–174.
46. Clore GM et al., Measurement of Residual Dipolar Couplings of Macromolecules Aligned in the Nematic Phase of a Colloidal Suspension of Rod-Shaped Viruses. *J Am Chem Soc* 1998;120:10571–10572.
47. Hansen MR et al., Tunable alignment of macromolecules by filamentous phage yields dipolar coupling interactions. *Nat Struct Biol* 1998;5:1065–1074.
48. Ruckert Man and Otting G., Alignment of biological macromolecules in novel nonionic liquid crystalline media for NMR experiments. *J Am Chem Soc* 2000;122:7793–7797.
49. Saas HJ et al., Solution NMR of proteins within polyacrylamide gels: Diffusional properties and residual alignment by mechanical stress or embedding of oriented purple membranes. *J. Biomol. NMR* 2000;18: 303–309.
50. Prestegard JH et al., Residual dipolar couplings in structure determination of biomolecules. *Chem Rev* 2004;104:3519–3540.
51. Schwieters CD et al., Using Xplor–NIH for NMR molecular structure determination. *Progr Nucl Magn Reson Spect* 2006;48: 47–62
52. Clore GM and Venditti V., Structure, dynamics and biophysics of the cytoplasmic protein–protein complexes of the bacterial phosphoenolpyruvate: sugar phosphotransferase system. *Trends Biochem Sci* 2013;38:515–530.

6. 국문초록

핵자기 공명 분광학을 이용한 마니톨 운반 효소 II의 도메인 A와 B의 상호작용에 관한 생물리학적 특성 연구

서울대학교 대학원

농생명공학부 바이오모듈레이션 전공

이고은

단백질 연결고리는 다중 도메인 단백질을 연결하여 개별 도메인이 일정한 거리 내에 있도록 하고, 도메인-도메인 움직임에 영향을 준다. 세포질단백질인 마니톨 운반 효소의 A 와 B 도메인은 미생물 종간 염기서열이 보존되어 있다. 중온성 세균 *Escherichia coli* 종에서 도메인 A 와 B는 유연한 연결고리로 공유결합으로 연결되어 있는 반면에 호열성 세균 *Thermoanaerobacter Tengcongensis* 종에서는 연결이 되어 있지 않다. 본 연구에서는 *Tt*종의 마니톨 전달 효소 도메인 A (*Tt*IIA^{mtl})와 인산화된 마니톨 전달 효소 도메인 B (phospho-*Tt*IIB^{mtl})의 구조와 상호작용을 통하여 도메인의 연결고리가 존재하거나 존재하지 않은 채로 진화되는 도메인 간의 상호작용 차이에 대하여 조사하였다. 각 도메인의 단백질 골격의 접힘 상태와 상호작용면은 두 미생물 종에서 잘 보존되어 있다. 그러나 연결고리가 존재하지 않는 도메인 간의 상호작용이 연결된 종보다 28배 강하게

나타났다. 복합체의 골격 접힘이 거의 변화하지 않은 채로 친화력이 증가한 주요 원인은 마니톨 전달 효소 도메인 A 의 상호작용면이 상이한 아미노산 잔기 조성을 가짐에서 비롯되었다. 마니톨 전달 효소 도메인 B의 루프의 활성 부위가 인산화되면서 상호작용면의 구조적 동역학을 감소시켜, 친화력 강화하는 중요 역할을 하였다. 상호작용면의 주요 잔기를 돌연변이시킨 단백질들을 통하여 친화력 강화에 대하여 설명하였다. 특히 돌연변이 된 IIA^{mtl}와 phospho-IIB^{mtl} 복합체는 IIA^{mtl}의 T542I와 P543T를 통하여 소수성 상호작용면이 확장되고, V557S의 하이드록실기와 IIB^{mtl} A386의 카르복실기가 수소결합을 이루어 안정적인 복합체가 된다. 이를 통하여 연결고리가 없음에도 도메인의 모임이 적합하게 이루어지도록 친화력이 강화를 설명할 수 있다. 흥미롭게도 생체 내에서의 도메인 모임의 확률이 연결고리가 있는 경우와 없는 경우에 매우 유사한 수준임을 알 수 있다. 그러므로 도메인 간의 친화력은 연결고리의 변화에 대응하여 진화하였음을 알 수 있고, 이는 도메인 모임이 연결고리와 관계 없이 기능을 유지할 수 있도록 돕는다.

주요어 : 도메인 상호작용, 도메인 접촉면, 마니톨 운반효소 II, 연결고리, 다중도메인 단백질, 핵자기공명 분광학,

학 번 : 2010-30826